

# FPGA-based hyperspectral lossy compressor with adaptive distortion feature for unexpected scenarios

Julián Caba, Dirk Stroobandt, María Díaz, Jesús Barba, Fernando Rincón,  
Sebastián López, *Member IEEE*, and Juan Carlos López, *Member IEEE*

**Abstract**—Lossy compression solutions have grown up during the last decades because of the increment of the data rate in the new-generation hyperspectral sensors, however linear compression techniques include useless information on regions of little interest for the final application and at the same time scarce information on areas of interest. In this paper, a transform-based lossy compressor, HyperLCA, has been extended to include a runtime adaptive distortion feature that brings multiple compression ratios in a same scenario. The solution has been designed to keep the same hardware-friendly feature, just like its previous version, specifically conceived to ease the deployment of the solution on reconfigurable hardware devices (FPGAs). The experiments demonstrate that the new version of the compressor is able to process 1024x1024 hyperspectral images and 180 spectral bands (377.5MB) in 0.935 seconds with a power consumption of 1.145 watts. In addition, experimental results also reveal that our architecture features high throughput (MSamples/s) and remarkable energy-efficiency (MB/s per watt) trade-offs, 10× and 6× greater than the best state-of-the-art solution, respectively.

**Index Terms**—hyperspectral imaging, lossy compression, on-board processing, FPGA, adaptive computing

## I. INTRODUCTION

THE information collected by hyperspectral sensors in the electromagnetic spectrum provides richness of spectral information, especially if they are high-resolution and multichannel, to be processed by applications related to the earth's observation. This fact makes hyperspectral technology a leading candidate for the analysis of land areas and, hence, has acquired an important relevance, being widely used for a variety of remote sensing applications such as precision agriculture, geological mapping or mineral exploration. Nevertheless, the large amount of data collected by these sensors requires huge on-board storage resources or high bandwidth communications, but both are limited. On top of that, the technological advances promote to market sensors with higher spectral and spatial resolutions that make on-board data processing more challenging [1], [2].

Traditionally, the information captured by hyperspectral sensors are not processed on-board due to the low computing performance and the limited on-board power capacity. Thus,

low-power and cost-optimized devices are selected to process the data sensed, but these devices do not feature a high performance [3]. In this regard, images are downloaded to the Earth's surface to be processed off-line by high-performance computing systems. In aerial capturing platforms, such as Unmanned Aerial Vehicles (UAVs), images are usually stored on-board and processed when the flight mission is completed [4]. Recently, some efforts have been made to transmit the images to the ground as soon as they are captured, but it requires a point-to-point connection with high bandwidth in order to reduce large delays [5]. Consequently, the transfer of large volumes of data reveals a bottleneck in the downlink systems that can affect the overall performance, as well as the budget of energy consumed by the transmission [6].

Recent studies propose edge computing solutions that allows to process the sensed images on-board by reducing the amount of downlink bandwidth. Most hyperspectral imaging applications requires the processing of huge data using complex algorithms with a formidable computational burden [7], whose solution is only feasible by the use of massive parallel processing architectures, such as Graphics Processing Units (GPUs) and Field-Programmable Gate Arrays (FPGAs), due to the performance they can achieve and the accuracy of the results obtained, even when fixed-point operations are used [2], [8], [9]. However, hyperspectral imaging applications are computationally intensive, included AI (Artificial Intelligence) models, since they require a high number of operations per second [10]. Unfortunately, most studies introduce high-performance devices to deploy FPGA or GPU-based solutions [11], [12], [13] that is generally not acceptable in mobile embedded systems, such as UAVs, owing to the power consumption constraints due to the difficulty of heat dissipation and the low power budget.

In this sense, the use of AI models with particular focus on Deep Neural Networks (DNNs) allows the deployment of value-added applications which utilize a tiny fraction of the downlink bandwidth that would be otherwise required [14]. Existing FPGA-based AI accelerators mostly tend to increase array scale to improve throughput performance by using large FPGA devices [15], [13], but few works optimize the hardware resource utilization. The widespread adoption of AI opens up the building of Commercial Off-The-Shelf (COTS) hardware accelerators for these algorithms, such as Myriad X Visual Processing Unit (VPU) [16] and Coral Tensor Processing Unit (TPU) [17], which feature high energy-efficiency and remarkable performance, cost, and mass trade-offs [18]. Furthermore, the open-source community facilitates

J. Caba, J. Barba, F. Rincón and J.C. López are with School of Computer Science, University of Castilla-La Mancha, 13071 Ciudad Real, Spain. E-mail: [julian.caba, jesus.barba, fernando.rincon, juanCarlos.lopez]@uclm.es.

D. Stroobandt is with Ghent University, 9000 Ghent, Belgium. E-mail: dirk.stroobandt@ugent.be.

M. Díaz and S. López are with the Institute of Applied Microelectronics (IUMA), 35017 Las Palmas de Gran Canaria, Spain. E-mail: [mddmartin, seblopez]@iuma.ulpgc.es.

Manuscript received January 6, 2023; revised MONTH DAY, YEAR.

the speed up of the deployment of the model, reducing the development time and costs with an acceptable level of reliability. Although COTS hardware accelerators are a technology that has burst onto the embedded systems, concretely in edge computing domain, the aforementioned trade-offs obtained by these devices are still slightly worse than ones provided by an efficient massive-parallel processing architecture based on FPGA technology due to COTS hardware accelerators are general purpose devices rather than domain specific [19].

Since the bandwidth is limited, as well as the in-circuit memory and dedicated hardware resources, such as DSPs, available on devices to implement a cost and energy-optimized solution, the way to address this challenge is to use on-board hyperspectral image compression techniques. Although there are a large variety of compression algorithms in the literature, lossless compression algorithms are preferred because they preserve most hyperspectral information [2]. Lossless techniques produce undistorted data after the decompression process, but the compression ratio is not large enough, however near-lossless methods allow obtaining larger values of compression ratio, introducing distortions that can be controlled in accordance with the compression ratio, but it can still be too small. Nevertheless, the latest-generation sensors increase the data-rate, requiring a higher compression ratio and real-time compression to avoid the accumulation of uncompressed data and therefore efficient transmission [20]. Although most state-of-the-art lossless compressors achieve a quite rate-distortion performance, they provide very moderate compression ratios roughly 2~3:1 [21], which are not enough to process the amount of data produced by newest-generation sensors. Therefore, limited communication bandwidths and increasing data volumes force to move from (near-)lossless compression techniques to lossy compression techniques, where a major research effort has been carried out in recent years [2], [22].

In mobile-embedded systems scenarios, parallel processing devices, such as cost-optimized FPGAs, are suitable to implement hyperspectral image compression algorithms, because of the balance between the degree of parallelism and the cost-energy, plus the cost savings of an FPGA-based solution with few resources. Unfortunately, the limited computational resources of these devices poses a new challenge when a solution is based on such technologies, so low-complexity compression schemes stand as the most practical solution for such restricted scenarios [23], [24]. Nevertheless, most state-of-the-art lossy compressors are based on existing 2D images or video compression algorithms, which are considered high computational burden, intensive memory requirements and non-parallel nature [25]. This fact causes its use to be limited in resource-constrained environments, such as on-board compression [26]. In this context, the Lossy Compression Algorithm for Hyperspectral Image Systems (HyperLCA) [27] has been developed as a hardware-friendly lossy compressor for hyperspectral images, which provides good compression ratios with a reasonable computational burden, because the compression process is based on transform operations. Briefly, this process maps the spatial domain of an image into its transformation domain to obtain the coefficients with larger amplitude, i.e., the features more representative of an image, which

are then encoded. In addition, this algorithm has been designed to meet the constraints imposed by pushbroom/whiskbroom scanners, considering each block independently, which results in less use of hardware resources. Its suitability for real-time performance applications has been previously analyzed in [28].

Nevertheless, HyperLCA and state-of-the-art lossy compressors behave linearly in compression ratio and quality performance terms, i.e. the hyperspectral data is compressed in accordance with a criteria that is defined at the beginning of the process and it does not change until it is completed. Such criteria defines the compressed image quality as well as the computational resources used in the compression process. Concretely, Signal-to-Noise Ratio (SNR), Root Mean Square Error (RMSE) and Maximum Absolute Difference (MAD) are conventional metrics applied in lossy image compression to describe the efficiency of compression and data quality for further use [29].

In this paper, the HyperLCA algorithm has been extended in order to include adaptive distortion feature without adding an overhead from the original implementation, making it a smart compressor by selecting the relevant blocks close to a pre-defined signature pattern. Therefore, the algorithm has been adapted to be run more flexibly with different compression ratios without modifying the set of core operations performed in its original version. Furthermore, an analysis of the FPGA-based HyperLCA with adaptive distortion feature has been carried out by setting different rules of the distortion applied on the same scenario, resulting in multiplicity of compression ratios within the same image and wide range of quality compression performance. It means multiplicity rate-distortion relations take place in the compressed image, which contains high and low rate distortions, so not only the most different hyperspectral pixels are perfectly preserved; that is, these pixels are within the extracted information along with extra relevant pixels of interesting blocks, which results in negligible losses since some compressed blocks have less distortion. This fact benefits many hyperspectral imaging applications in which the spectral resolution is decisive; the blocks containing a large number of similarities can be compressed with a different criteria than blocks with lower similarities to the pattern. The relevant blocks are selected at run-time by comparing pixel by pixel with a signature pattern looking for similarities in each of the spectrum bands. Finally, the architecture has been compared with the previous version implemented in [8] and other state-of-the-art compressors in terms of throughput and hardware resource utilization. Against this backdrop, the major motivation of this work is to demonstrate the aforementioned claims about the HyperLCA with quality control, and therefore, the aim is to contribute to the scientific community with an intelligent lossy compressor for hyperspectral imaging, which enriches those blocks of greatest interest in an unexpected/unknown scenario, by using a cost-optimized and energy-efficient solution based on FPGA technology.

This paper is organized as follows. Section II explains in detail the proposed quality control version of the HyperLCA compressor and highlights the differences with its original version. Section III includes a comprehensive description about the FPGA-based architecture for the execution of the com-

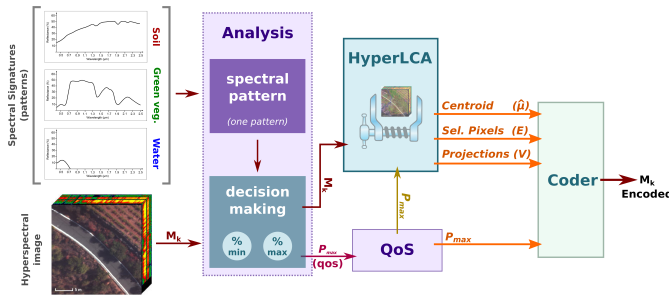


Fig. 1. Overview of the HyperLCA compressor with adaptive distortion.

pressor. The results of the proposed hyperspectral compressor implemented on a ZC7Z020 FPGA device have been evaluated in Section IV. Section V discusses about the performance and hardware resources utilization of the proposed architecture. Finally, Section VI shows conclusions achieved in this work.

## II. HYPERLCA ALGORITHM

The HyperLCA algorithm is a lossy transform-based compressor for hyperspectral imaging, whose original version has been modified into a hardware-friendly version. Thus, the algorithm has been redesigned to achieve high compression rate-distortion ratios, as well as the computational burden has been decreased due to the high-level of parallelism implemented for applications based on pushbroom/whiskbroom sensors [9]. All of the changes made allow for the use of parallel processing architectures, such as GPUs or FPGAs, on which the algorithm has been implemented, [28] and [8], respectively. Moreover, HyperLCA algorithm have been specially designed to work inside specific numeric ranges and use integer arithmetic, specifying the precision needed for the operations to be suitable in parallel computing architectures as previously discussed in [8], [9], [28].

The transform-based proposed solution can independently process blocks of the image regardless of the spatial alignment of them, which facilitates the parallelization of the compression process. It means that a hyperspectral pixel can be processed independently of the subsequent pixel. On this basis, this paper proposes to analyze each pixel at run-time to determine the rate of distortion that should be applied to the block being processed, rather than setting a desired minimum compression ratio for all blocks captured by the sensor, as previous versions of the algorithm perform. Figure 1 shows an overview of the new version of the algorithm that represents the three main computing stages involved in the HyperLCA compressor with adaptive distortion feature, composed by a pre-processing or block analysis stage, a spectral transform stage and an entropy coding stage.

### A. Stage 1: Pre-processing or block analysis

Firstly, the hyperspectral image is broken into blocks composed of  $BS$  consecutive horizontal pixels ( $\mathbf{M}_k$ ), also known as lines or blocks, that will be processed. Then, the  $p_{max}$  most representative pixels within a block ( $\mathbf{M}_k$ ) are calculated; it is feasible because the HyperLCA compressor follows the

unmixing-like strategy. The previous implementations of the HyperLCA algorithm initialize the  $p_{max}$  parameter from three input parameters:  $CR$  (minimum desired compression ratio),  $N_{bits}$  (number of bits) and  $BS$  (block size) to determine the number of transformations performed on the hyperspectral block. However, in this work, the  $p_{max}$  is not fixed at design time, it is recalculated for each block regarding to the number of similar pixels with a hyperspectral pattern signature. The balance between SNR, RMSE and MAD quality metrics has been previously evaluated in earlier publications by combining different configurations of the input parameters ( $CR$ ,  $N_{bits}$  and  $BS$ ) [28]. In particular, one of the best configurations is set the  $N_{bits}$  and  $BS$  parameters to 12 and 1024, respectively. These values are kept to calculate the  $p_{max}$  at run-time, whilst the  $CR$  depends on the number of hyperspectral pixels close to the pattern signature.

Therefore, the HyperLCA compressor determines the number of transformations performed on the block being processing,  $\mathbf{M}_k$ , as shown in Equation (1), where  $DR$  refers to the number of bits per pixel per band;  $nb$  represents the number of bands;  $BS$  is the number of consecutive horizontal pixels in a single block;  $CR$  refers to the desired compression ratio, defined as the relation between the number of bits in the original image and the ones of the compressed data; and  $N_{bits}$  is the number of bits that determines the precision and dynamic range to be used for representing the values of the compressed data. Thus, the number of transformations performed,  $p_{max}$ , directly determines the maximum compression ratio to be reached with the selected configuration, in which higher  $p_{max}$  values result in better reconstructed images, but lower compression ratios.

$$p_{max} \leq \frac{DR \cdot nb \cdot (BS - CR)}{CR \cdot (DR \cdot nb + N_{bits} \cdot BS)} \quad (1)$$

The compression ratio ( $CR$ ) used in the calculation of  $p_{max}$  for a block must be determined by analyzing each of the pixels of that block ( $\mathbf{M}_k$ ), comparing them one by one with a reference hyperspectral signature (reference pattern). This process can be done by using the Euclidean distance with the reference signature and the hyperspectral pixels within a block to determine if the block, which is being processed, contains a high percentage of pixels close to the reference or, on the contrary, contains few matches. However, Euclidean distance calculation is costly in reconfigurable devices and makes it necessary to look for alternatives. In this sense, this work proposes a hardware-friendly solution by the use of band-limit values, where a *delta* value is defined to set the upper and lower limits that draw the same plot that the reference signature. The results of this method are similar to the ones obtained by Euclidean distance method.

Figure 2 shows graphically the band-limit adopted approach, where three hyperspectral pixels and a reference signature (black line) are plotted. In addition, the red dotted lines define the upper and lower limits whose trend is identical to that drawn by the reference signature. Therefore, hyperspectral signatures within both limits are considered close to the

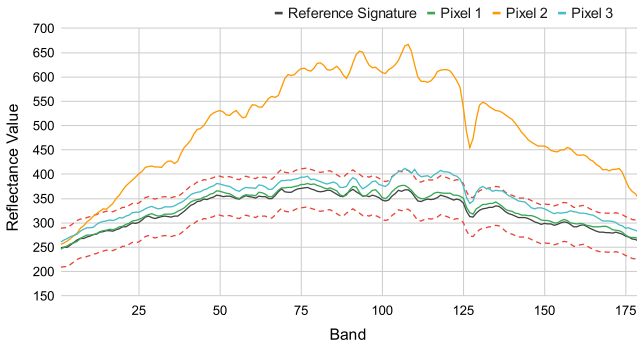


Fig. 2. Overview of pixel selection process by limits.

reference (green line of Figure 2), as well as those pixels whose a few number of reflectance values are outside the limits (blue line of Figure 2); the number of values outside the limits is configurable. This fact means that hyperspectral signatures whose reflectance is very similar to the reference, except in a small number of bands, are also considered to be close to the reference signature. Meanwhile, the hyperspectral pixels whose most reflectance values are outside the limits are not considered (orange line of Figure 2).

Once all hyperspectral pixels within a block are defined as in or out the limits, the  $CR$  is set by analyzing the number of pixels inside the boundaries. Figure 3 shows three examples with different compression ratios over the same scenario. Firstly, Figure 3a is an original RGB figure of a vineyard scenario, whilst Figure 3e shows a pattern in which white and black colors represent the green vegetable signatures and other materials, respectively. Unfortunately, the sensor used in this work captures the hyperspectral information line by line, it means the whole hyperspectral information of a scenario is not obtained immediately, so the operations must be performed over a line ( $\mathbf{M}_k$ ) with  $BS$  hyperspectral pixels. Thus, when a low distortion is required but only in the blocks which contains useful information for the final application, the number of hyperspectral pixels close to the reference must be small. In this sense, Figures 3b 3c and 3d highlight in green the blocks whose  $CR$  is low, i.e. these lines contain useful information for the final application, while the blocks whose hyperspectral information is not too relevant are highlighted in black. Meanwhile, Figures 3f, 3g and 3h highlight the loss, hit and excess of hyperspectral information with respect to the ideal information extraction (Figure 3e) in white, green and red, respectively. The process to select relevant blocks in the different scenarios fulfills the following criteria: at least 10 pixels close to the reference for the scenario represented in Figure 3b, at least 300 pixels close in the case of Figure 3c and at least 800 pixels in the last case (Figure 3d).

### B. Stage 2: Spectral transform

The HyperLCA compressor is among the transform-based algorithms that employs a modified version of the well-known Gram-Schmidt orthogonalization method, which is widely used in lossy compression because of its moderate complexity, in which no band reordering is required. The basic idea of

### Algorithm 1 HyperLCA Transform.

**Inputs:**

$$\mathbf{M}_k = [\mathbf{r}_1, \mathbf{r}_2, \dots, \mathbf{r}_{BS}], p_{max}$$

**Outputs:**

$$\hat{\boldsymbol{\mu}}; \mathbf{E} = [\mathbf{e}_1, \mathbf{e}_2, \dots, \mathbf{e}_{p_{max}}]; \mathbf{V} = [\mathbf{v}_1, \mathbf{v}_2, \dots, \mathbf{v}_{p_{max}}]$$

**Algorithm:**

- 1: Average pixel:  $\hat{\boldsymbol{\mu}}$ ;
- 2: Centralized image:  $\mathbf{C} = \mathbf{M}_k - \hat{\boldsymbol{\mu}} = [\mathbf{c}_1, \mathbf{c}_2, \dots, \mathbf{c}_{BS}]$ ;
- 3: **for**  $n = 1$  **to**  $p_{max}$  **do**
- 4:     **for**  $j = 1$  **to**  $BS$  **do**
- 5:         Brightness Calculation:  $\mathbf{b}_j = \mathbf{c}'_j \cdot \mathbf{c}_j$ ;
- 6:     **end for**
- 7:     Maximum Brightness:  $j_{max} = \text{argmax}(\mathbf{b}_j)$ ;
- 8:     Extracted pixels:  $\mathbf{e}_n = \mathbf{r}_{j_{max}}$ ;
- 9:      $\mathbf{q}_n = \mathbf{c}_{j_{max}}$ ;
- 10:      $\mathbf{u}_n = \mathbf{q}_n / b_{j_{max}}$ ;
- 11:     Projection vector:  $\mathbf{v}_n = \mathbf{u}'_n \cdot \mathbf{C}$ ;
- 12:     Information Subtraction:  $\mathbf{C} = \mathbf{C} - \mathbf{q}_n \cdot \mathbf{v}_n$ ;
- 13: **end for**

this class of algorithms is to map the spatial domain of a hyperspectral image into its transformation domain [2]. In this regard, the *Spectral Transform* stage selects the most different pixels of a hyperspectral image using orthogonal projection techniques. Therefore, the selected pixels are used for projecting the image in order to remove redundancies and thus obtain a spectral decorrelated and compressed image.

The *Spectral Transform* applied by HyperLCA compressor is described in detail in Algorithm 1. The inputs of this stage are the hyperspectral block to compress ( $\mathbf{M}_k$ ), which is the same as the one being analyzed by the *Pre-processing* stage, and the number of most different pixels to extract ( $p_{max}$ ), which is the output of the *Pre-processing* stage, i.e. it is responsible for determining the number of transformations or orthogonal projections to perform on the hyperspectral block. Whilst the outputs of this stage are the average pixel ( $\hat{\boldsymbol{\mu}}$ ) of the input hyperspectral block ( $\mathbf{M}_k$ ), the set of indexes related to the  $p_{max}$  most different hyperspectral pixels ( $\mathbf{E}$ ) and their corresponding projection vectors ( $\mathbf{V}$ ).

The first step of the algorithm is to centralize the hyperspectral block ( $\mathbf{M}_k$ ) subtracting the average pixel ( $\hat{\boldsymbol{\mu}}$ ), which is obtained by adding all the pixels of a band of the hyperspectral block and dividing by the number of pixels ( $BS$ ), this operation is performed for all the bands of the block, resulting in a vector with  $nb$  (number of bands) elements (line 1 of Algorithm 1). Then, it is used to get the centralized version of the hyperspectral block ( $\mathbf{C}$ ) in line 2. In a second step, the  $p_{max}$  most characteristic pixels are sequentially extracted from lines 3 to 13. For this purpose, the brightness of each hyperspectral pixel within the block is calculated following a vector normalization strategy, which is defined as the product of each band within the hyperspectral pixel with itself (lines 4 to 6 of Algorithm 1). Subsequently, the highest brightness ( $j_{max}$ ) in each iteration determines the pixels to extract ( $\mathbf{e}_n$ ) from the original hyperspectral block ( $\mathbf{M}_k$ ), so the algorithm searches



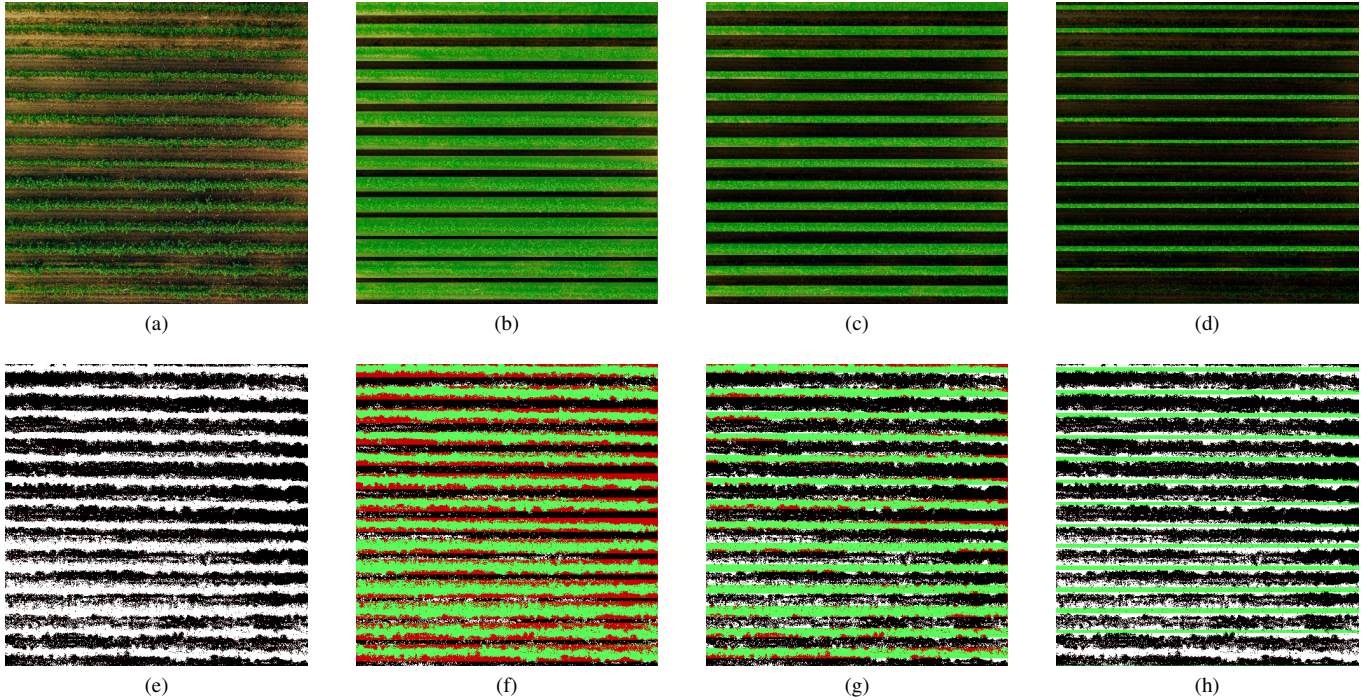


Fig. 3. Pixel selection in a vineyard scenario (selected blocks in green color). (a) Original Vineyard. (b) Line selection with low compression ratio. (c) Line selection with mid compression ratio. (d) Line selection with high compression ratio. (e) Pattern of pixel selection. (f) Differences between selected pixels in (b) and pattern. (g) Differences between selected pixels in (c) and pattern. (h) Differences between selected pixels in (d) and pattern.

for the maximum value of the previously calculated brightness and then extracts the original pixel whose index matches this maximum brightness, such operations are performed in lines 7 and 8 of Algorithm 1, respectively. Afterwards, the orthogonal vectors,  $\mathbf{q}_n$  and  $\mathbf{u}_n$ , are obtained (lines 9 and 10);  $\mathbf{q}_n$  is the hyperspectral pixel of the block ( $\mathbf{M}_k$ ) whose brightness value is the highest, while  $\mathbf{u}_n$  is obtained by dividing each value of  $\mathbf{q}_n$  by the brightness value. The projection of each block pixel over the direction spanned by the selected pixel is estimated with  $\mathbf{u}_n$  orthogonal vector (line 11 of Algorithm 1). Finally, the extracted information is subtracted from the centralized block  $\mathbf{C}$  in line 12, resulting in a new hyperspectral block, also called  $\mathbf{C}$ , that is the new input of the loop block.

Accordingly,  $\mathbf{C}$  retains the spectral information that is not represented by the extracted pixels ( $\mathbf{E}$ ) and thus it also represents the information that will be not recovered in the decompression process. Therefore, highest  $p_{\max}$  values reduces the information that cannot be recovered. In this sense, the adaptive distortion feature mitigates the lost of information in the relevant blocks for the final application, so higher  $p_{\max}$  values are applied in those blocks.

### C. Stage 3: Entropy coding

The last stage of the HyperLCA compressor performs the entropy-coding of the vectors received from the *Spectral Transform* stage, where the use of Golomb-Rice algorithm [30] makes possible to consider each vector independently from the rest, i.e. the outputs of *Spectral Transform* stage can be consumed as they are received, thus both stages are carried out in parallel. To do so, the compression parameter ( $N$ ) is

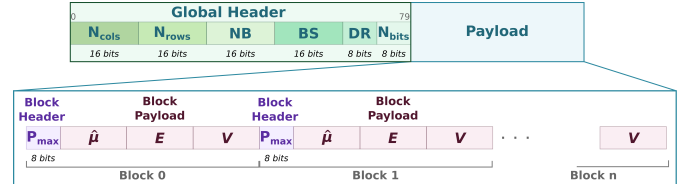


Fig. 4. Overview of the bitstream structure generated.

calculated as the average value of the vector being processed. Afterwards, the elements of the vector are divided by  $N$  as well as the quotient ( $q$ ) and the remainder ( $r$ ) of such operation are also obtained. Second, the lowest power of 2 higher than  $N$  is calculated as  $b = \log_2(N) + 1$ . The quotient ( $q$ ) is codified using unary code, whilst the remainder ( $r$ ) is coded as plain binary using  $b - 1$  bits for  $r$  values smaller than  $2^b - N$ , otherwise it is coded as  $r + 2^b - N$  using  $b$  bits.

### D. Bitstream Generation

Finally, *Data Packaging* stage is performed to generate a unique bitstream that contains the outputs of the aforementioned compression stages. Figure 4 graphically shows the structure generated for the compressed bitstream, which is divided into two hierarchical blocks.

Firstly, a *Global Header* takes place at the beginning of the stream to define the global information about the hyperspectral image, including the parameters used in the compression process. It contains the spatial (number of columns and rows) and spectral (number of bands) information of the processed image, it also denotes the block size used ( $BS$ ), the number

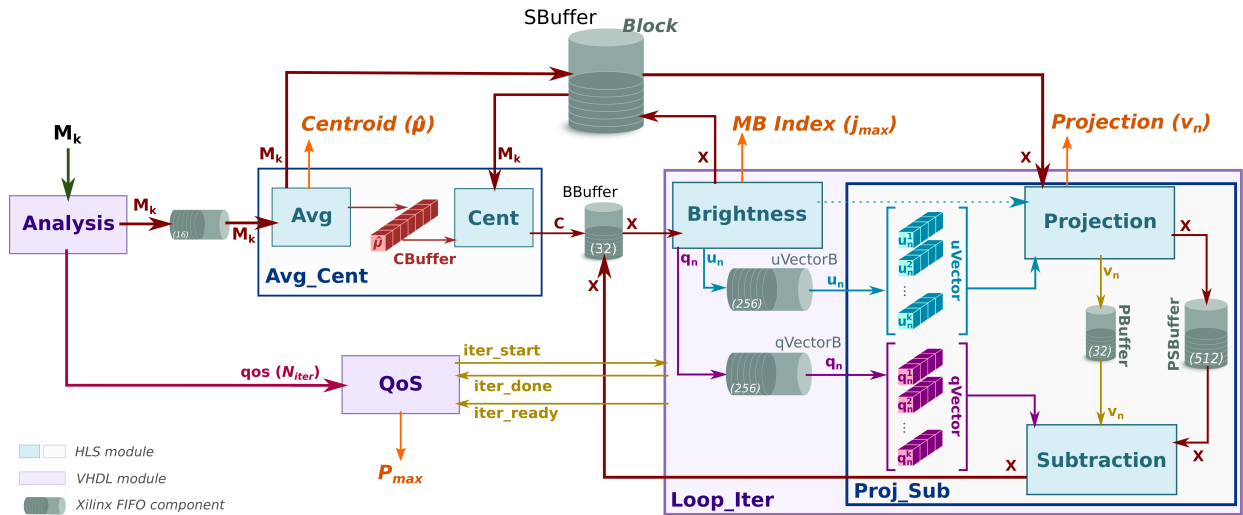


Fig. 5. Overview of the hardware implementation related to the HyperLCA transform with quality control.

of bits per pixel per band ( $DR$ ) and the number of bits used for representing the values of the compressed data ( $N_{bits}$ ).

The payload is placed after the *Global Header*, which is broken into blocks that contains two fields: *Block Header* and *Block Payload*. Owing to the fact that the blocks of a hyperspectral image are compressed with a variety number of transformations, it is mandatory an 8-bit header to determine the  $p_{max}$  applied in each block. After the *Block Header*, there is the *Block Payload* which is composed of a single centroid regardless of the distortion applied on the block and then the vectors  $\mathbf{E}$  (most different pixels) and  $\mathbf{V}$  (projections), whose number is denoted by the aforementioned 8-bit header.

### III. FPGA IMPLEMENTATION OF HYPERLCA ALGORITHM

The HyperLCA compressor with adaptive distortion feature has been implemented on reconfigurable hardware using HLS (High-Level Synthesis) to define each operation involved in the HyperLCA algorithm as a set of specialized hardware accelerators. HLS reduces the development lifecycle due to the use of High-Level Languages (HLLs), such as C or C++, to describe the functionality and include features that allow to optimize and improve the functionality described by non-hardware engineers [31].

In this work, specialized hardware accelerators have been reused from [8] to build the new architecture of the HyperLCA transform, adding the dynamic behavior required to include multiple compression ratios. Figure 5 shows an overview of the hardware architecture implemented for *pre-processing* and *spectral transformation* stages, where the blue boxes correspond to the modules described in HLS, and are therefore inherited from the previous development. These modules are connected through memory buffers and custom logic that orchestrates them to obtain the desired behavior. For the sake of clarity, the matching of the blue boxes with the operations performed in Algorithm 1 is as follows: *Avg\_Cent* corresponds to lines 1 and 2, while *loop\_iter* is the main loop body that comprises from line 3 to 13, where *brightness* is calculated in the inner loop and line 7 of Algorithm 1, orthogonal vectors

( $\mathbf{q}$  and  $\mathbf{u}$ ) are also obtained once the brightest pixel is selected. Meanwhile *projection* and *subtraction* match with lines 11 and 12 of Algorithm 1, respectively. In pursuit of improving the performance, the architecture introduces an enhancement through the partitioning of the orthogonal vectors,  $\mathbf{q}$  and  $\mathbf{u}$ , using VHDL instead of applying a pragma directive on the HLS description, just before they are used by the *projection* and *subtraction* modules.

Up to this point, the described architecture is responsible to carry out the transformation process on the hyperspectral blocks ( $\mathbf{M}_k$ ). However, the transform-based operations carried out, i.e., the number of executions of the *loop\_iter* module, is now calculated at run-time. The number of iterations is related to the compression ratio applied to a block, which also means the amount of hyperspectral data is represented for each block. Thus, the *QoS* module manages this process, as well as notifies the  $p_{max}$  value used to encode the current hyperspectral block ( $\mathbf{M}_k$ ). In contrast, the *Analysis* module is in charge of calculating the number of iterations to be performed according to the similarity between the pixels that compose a hyperspectral block and the pattern signature.

Therefore, the *Analysis* module corresponds to *Stage 1* (pre-processing) and it is the first operation to be executed before performing any transformation. In fact, the block analysis process and the first operation of the *spectral transform* stage (i.e. the calculation of the average pixel) work in parallel. To do so, the *Analysis* module makes a copy of the hyperspectral block ( $\mathbf{M}_k$ ) in batch mode as soon as it receives the block, so the *Avg* module can begin to process it. The parallelism of both operations allows to obtain the number of transformations to be applied to the current hyperspectral block with a negligible overhead and it does not block the HyperLCA operations. Focusing on the hardware implementation of the *Analysis* module, the operations performed by this module has been segmented into a four-stage pipeline and an additional decision-stage that determines the number of iterations ( $N_{iter}$ ) to apply in the *spectral transform* stage. Figure 6 shows an overview of the pipeline-based architecture, which has been implemented

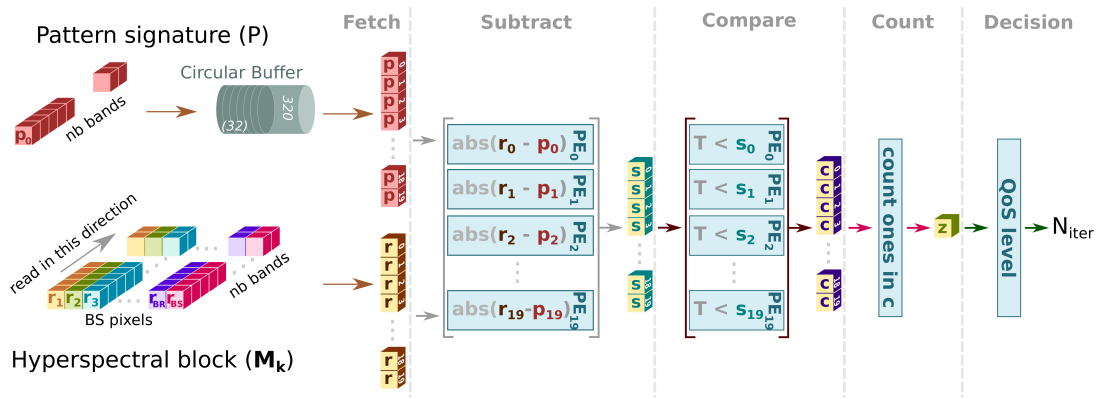


Fig. 6. Overview of pipeline-based architecture to calculate the number of transformations (Number of PEs = 20).

in VHDL and whose stages perform the following tasks.

**Fetch.** The data of the pattern signature ( $\mathbf{P}$ ) and hyperspectral block ( $\mathbf{M}_k$ ) is read in batch mode and stored in  $p_i$  and  $r_i$  registers, respectively (see Figure 6). Thus, this stage reads as many bands as can be processed in parallel by the operators of the *spectral transform* stage, e.g., 20 processing elements (PE) are required to process 20 spectral bands in parallel. In this sense, the word widths of the internal memories/registers of the architectures shown in Figure 5 and 6 must be configured to work with the corresponding number of bands. On top of that, the pattern signature, which is previously stored in a ROM, is moved to a circular buffer before being retrieved; this process is performed before the *fetch* stage and it is done to save time and improve the performance, because the pattern must be used the same number of times as the number of hyperspectral pixels contained in the captured image, i.e. the pattern signature is read  $BS$  times in a hyperspectral block ( $\mathbf{M}_k$ ) and repeated by the lines that contain the hyperspectral image.

**Subtract.** Once the hyperspectral data is ready, the *subtract* stage subtracts from the current hyperspectral block ( $\mathbf{M}_k$ ) the pattern signature by bands, so that the first band of the hyperspectral pixel belonging to the processed block is subtracted by the first band of the stored pattern, then the second band of both and so on. These operations are also performed in parallel. Finally, the absolute value of the operation is also calculated. The results of this stage are stored in  $s_i$  registers, which are represented as yellow and green boxes in Figure 6.

**Compare.** The results obtained from each PE in the *subtract* stage are compared with a constant value,  $T$ , which is the predefined *delta* value. Thus, if the constant  $T$  is smaller than the result of the absolute subtraction obtained in the previous stage, it means that the corresponding band is within the limits. On the other hand, if the comparison results that  $T$  is greater, it implies that the value of the band is outside the limits. The output of this stage is a zero or one when the band is outside or within the limits, respectively. In a similar way to the previous stage, the results of the comparisons are also stored in  $c_i$  registers (yellow and purple boxes in Figure 6).

**Count.** In this stage, the registers that contains a one, i.e. the band is within the limits, are counted and added to a partial sum, which is stored in  $z$  register (see Figure 6). Thus, this

register is updated until the hyperspectral pixel is compared with the pattern signature, then it is set to zero to compare the next pixel of the hyperspectral block.

Finally, the *decision* stage is performed after the whole hyperspectral pixel of a block is compared with the pattern signature. It determines whether a pixel is close to the pattern from the sum value stored in the  $z$  register and calculated by the *count* stage. In this sense, it is not necessary that all band values are within the limits, the solution allows several bands to be out of them (see blue line in Figure 2). On top of that, the *decision* stage sets the number of transform operations carried out by the *spectral transform* stage. It is calculated by counting the number of pixels close to the pattern signature ( $T_c$ ) and, then, compare such sum with the predefined user rules, which figures out the provided quality of service, i.e. the degree of distortion. To do that, the user must provide two constants  $R_{min}$  and  $R_{max}$  to apply the following cases, where  $QoS_{max}$ ,  $QoS_{min}$  and  $QoS_{med}$  are the number of iterations that are also predefined; a high number means greater spectral information extracted.

$$\begin{cases} N_{iter} = QoS_{max}, & \text{if } T_c \geq R_{max} \\ N_{iter} = QoS_{min}, & \text{if } T_c \leq R_{min} \\ N_{iter} = QoS_{med}, & \text{otherwise} \end{cases}$$

#### IV. RESULTS

The lossy compressor with adaptive distortion feature is evaluated in this section by analyzing the FPGA-based architecture implemented on a ZC7Z020-CLG484 and the performance achieved by it, comparing the throughput and power consumption when several PEs are working in parallel. This section also evaluates the accuracy of the limit method versus the use of Euclidean distance, which involves complex operations, such as square root operation, that demand high computational resources when it is developed in reconfigurable technology.

##### A. Hyperspectral dataset collected

The performance of the proposed FPGA-based architecture has been evaluated by a set of hyperspectral images, which were sensed by a custom aerial platform over different farming



areas on the island of Gran Canaria (Spain). The dataset contains 4 hyperspectral images collected over two different vineyard areas, whose exact coordinates are 27°59'35.6"N 15°36'25.6"W and 27°59'15.2"N 15°35'51.9"W. For analysis purposes, the dataset used in the previous work is kept [8].

The acquisition platform mounts a *Specim FX10* pushbroom hyperspectral camera on a DJI Matrice 600 drone [32]. The image sensor captures 1024 spatial pixels per track and up to 224 spectral bands in the range between 400 and 1000 nm. Nevertheless, the experiments performed only work with 180 spectral bands; the first 10 spectral bands are discarded as well as the last 34 bands. This fact is done because the response in the boundaries of the electromagnetic spectrum is low.

### B. Evaluation of the near pixel selection method

The goodness of the pixel selection method through upper and lower limits proposed in this work has been evaluated and compared with the Euclidean distance. For doing so, the analysis has been carried out using the Set Theory operations to determine the similarity of the results obtained from both solutions. Concretely, six different metrics have been applied to analyze the set of pixels selected by the method used in this work. It is worth mentioning that the result obtained, regardless of the method used, is a set of pixels that are similar to the reference pattern, and hence, the analysis must be driven by the similarities between result sets.

In this context, the universal set,  $\mathbf{U}$ , is composed by the index of pixels within a hyperspectral block ( $\mathbf{M}_k$ ). Thus,  $\mathbf{U}$  is defined as  $\mathbf{U} = \{0, \dots, 1023\}$  or  $\mathbf{U} = \{x \mid x \in \mathbb{N} \wedge x \leq 1023\}$ . The set of pixels selected by the Euclidean distance algorithm is denoted as  $\mathbf{E}$  ( $\mathbf{E} \subseteq \mathbf{U}$ ), whereas the ones extracted by the limit method is represented as  $\mathbf{L}$  ( $\mathbf{L} \subseteq \mathbf{U}$ ). The following lines describe the six metrics used to determine the degree of similarity of the two approaches.

**True Positives.** This metric analyzes the number of common pixels selected by the two algorithms, i.e. the intersection operation is applied to  $\mathbf{E}$  and  $\mathbf{L}$  sets, which are obtained by the Euclidean distance and the limit method, respectively (see Equation 2). Equation 3 calculates the percentage of hits in  $\mathbf{L}$  relative to  $\mathbf{E}$ ; a high percentage means that most pixels selected by the Euclidean distance are also chosen by the limit method, but it does not imply that they are very similar; the  $\mathbf{L}$  set may contain many more pixels than  $\mathbf{E}$  does not.

$$E \cap L = \{x \mid x \in E \wedge x \in L\} \quad (2)$$

$$n(E \cap L)/n(E) \quad (3)$$

**False Negatives.** In this case, it represents the pixels within  $\mathbf{E}$  but not in  $\mathbf{L}$ , or in other words, it denotes the pixels that the limit algorithm should have included in its solution set but are not actually included. The set of false negatives is extracted by the difference operation as Equation 4 shows, where the common pixels of  $\mathbf{E}$  and  $\mathbf{L}$  are extracted from  $\mathbf{E}$ . This metric and the true positive metric provide the degree of similarity between sets; a low percentage of false negatives and a high percentage of true positive means that two sets are very similar. Equation 5 calculates the percentage of pixels not considered by the limit method.

$$E - L = \{x \mid x \in E \wedge x \notin L\} \quad (4)$$

$$n(E - L)/n(E) \quad (5)$$

**False Positives.** This metric measures the degree of extra pixels considered by the limit method. It is also calculated by the difference operation, but now the common pixels of  $\mathbf{E}$  and  $\mathbf{L}$  are extracted from  $\mathbf{L}$  instead of  $\mathbf{E}$  (see Equation 6). A small percentage value of this metric implies that the solution is tight, whenever the true positives metric has a high value and the false negatives metric has a low value. The percentage of pixels included by the limit method is calculated in Equation 7.

$$L - E = \{x \mid x \notin E \wedge x \in L\} \quad (6)$$

$$n(L - E)/n(L) \quad (7)$$

**True Negatives.** In this case, the metric denotes the pixels not included in the solutions of both methods, i.e. the pixels that are not in  $\mathbf{E}$  nor  $\mathbf{L}$ . It is calculated by the union of  $\mathbf{E}$  and  $\mathbf{L}$  sets and then the result is subtracted (difference operation) from the universal set ( $\mathbf{U}$ ). Equation 8 shows the operations performed to obtain the set of pixel considered as true negatives, whilst Equation 9 shows the formula to calculate the success rate of this metric, where  $E'$  is the true negatives of the result obtained by the Euclidean distance algorithm.

$$U - (E \cup L) = \{x \mid x \in U \wedge (x \notin E \vee x \notin L)\} \quad (8)$$

$$n(U - (E \cup L))/n(E') \quad (9)$$

**E is a subset of L.** This metric determines whether the whole set obtained from the Euclidean distance algorithm is a subset of the set obtained by the limit method. It means that the solution contains all pixels that the reference algorithm.

**L is a subset of E.** In this case, it denotes the lack of pixels in the solution because the set obtained by the Euclidean distance algorithm is greater than the one obtained by the limit method. This metric and the above one are interesting to attend when a large number of pixels are analyzed, with two sets of pixels, this information can be extracted from the first four metrics.

Table I lists the percentage of similarity between the Euclidean distance and Limit methods to select the set of pixels close to the pattern signature. To do so, the set obtained by Euclidean method must be satisfied that none of the members of such set exceeds the value of 200 with respect to the distance to the reference. Meanwhile, the limit method defines the upper and lower boundaries according to the spectral values of the pattern signature with a unique variable (*limits* column of Table I), in addition, it also defines the maximum number of spectral bands whose values are outside the boundaries (*errors* column of Table I). These parameters are configurable and, for the current analysis, the selected values are listed in the two first columns of Table I.

Analyzing the results shown in Table I, the best configurations are those with a high percentage of true positives and a low percentage of false positives and negatives. In this sense, the configurations with 100% hits (true positives) have at the same time the highest percentage of false positives, so they



TABLE I  
COMPARISON OF RESULTS OBTAINED BETWEEN THE EUCLIDEAN DISTANCE AND LIMIT METHODS.

Limits	Errors	True Positives ( $E \cap L$ )	False Negatives ( $E - L$ )	False Positives ( $L - E$ )	True Negatives ( $U - (E \cup L)$ )	$E \subseteq L$	$L \subseteq E$
$\pm 15$	20	49.093%	50.906%	0.0000%	100.00%	0.6835%	100.00%
	25	54.467%	45.532%	0.0000%	100.00%	0.7812%	100.00%
	30	60.003%	39.996%	0.0077%	99.999%	1.0745%	99.804%
$\pm 20$	20	82.158%	17.841%	0.2145%	99.992%	6.3476%	93.261%
	25	89.024%	10.975%	0.9618%	99.963%	14.160%	73.339%
	30	94.686%	5.3133%	2.8799%	99.879%	28.711%	41.601%
$\pm 23$	20	96.843%	3.1564%	7.6101%	99.658%	42.187%	22.949%
	25	99.256%	0.7437%	12.146%	99.413%	76.172%	8.0078%
	30	99.958%	0.0418%	17.789%	99.074%	98.339%	2.6369%
$\pm 24$	20	98.703%	1.2969%	12.198%	99.413%	65.332%	11.230%
	25	99.823%	0.1766%	17.296%	99.106%	93.652%	3.0273%
	30	99.995%	0.0046%	22.758%	98.739%	99.804%	1.3671%
$\pm 25$	20	99.526%	0.4741%	16.796%	99.140%	85.156%	4.0039%
	25	99.944%	0.0557%	22.292%	98.773%	97.949%	1.5625%
	30	100.00%	0.0000%	27.498%	98.377%	100.00%	0.7812%
$\pm 26$	20	99.842%	0.1580%	21.478%	98.831%	94.443%	2.2461%
	25	99.991%	0.0093%	26.839%	98.430%	99.609%	0.8789%
	30	100.00%	0.0000%	31.697%	98.014%	100.00%	0.6836%
$\pm 27$	20	99.939%	0.0604%	25.837%	98.510%	97.754%	1.0742%
	25	100.00%	0.0000%	30.963%	98.081%	100.00%	0.6836%
	30	100.00%	0.0000%	35.542%	97.641%	100.00%	0.6836%
$\pm 30$	20	100.00%	0.0000%	37.044%	97.482%	100.00%	0.4883%
	25	100.00%	0.0000%	41.147%	97.008%	100.00%	0.3906%
	30	100.00%	0.0000%	44.861%	96.519%	100.00%	0.2929%

are not good candidates, e.g. the last limit configuration listed in the table. On the other hand, configurations with a low percentage of false negatives and an acceptable percentage of true positives are not good candidates either, for example the second configuration of the limits ( $Limits = \pm 20$ ) reaches up to 94.68% in true positives, but the value of the  $E \subseteq L$  metric is very low; 6.34%, 14.16% and 28.71% for 20, 25 and 30 *Errors* parameter configuration, respectively. Thus, it means that most of the obtained sets do not include all values obtained by the Euclidean distance method. Focusing on the rest of the configurations, the best configuration is the one whose *Limits* and *Errors* parameters are configured with  $\pm 25$  and 30, respectively. The obtained results with the aforementioned configuration contains all pixels acquired by the Euclidean distance, but extending the sets by including more pixels as it denotes the false positives metric. In addition, the second best configuration,  $Limits = \pm 24$  and *Errors* = 30, is also a very good candidate because of its balance between true positives and false positives. Therefore, the Limit method is a suitable candidate to replace the Euclidean distance method in reconfigurable devices due to the simplicity of the operations performed, as well as the similarity of the obtained results.

### C. Hardware analysis

The proposed architecture has been implemented on a ZC7Z020-CLG484 FPGA device for analysis purposes and with a twofold objective; firstly, the architecture is kept in order to compare this new version of the algorithm with the one previously implemented in [8], secondly the FPGA architecture (Artix) is a cost-optimized device compared to other architectures of the same manufacturer, such as Kintex or UltraScale/UltraScale+. In this sense, the selected device provides a good trade-off on three aspects: cost, power consumption and throughput. However, to achieve a good ratio balance in performance per watt, it is necessary to invest

engineering efforts in the architectural part as a consequence of the limited resources of the ZynQ SoC. For the sake of clarity, the hyperspectral images have been stored in an external memory (DDR) to analyze the performance of the developed architecture. Thus, the hardware accelerator reads the spatial and spectral information of the hyperspectral images from the DDR through an AXI-Stream interface using a DMA (Direct Memory Access).

Table II lists the programmable logic resources in accordance with the number of processing elements (*PE*) instantiated in each configuration after post-implementation phase, where the PEs work in parallel to process several bands in batch mode. The hyperspectral block size (*BS*) is set to 1024 hyperspectral pixels, whilst the spatial size is 180 bands. The number of *PEs* that can be instantiated is 20 *PEs*, since the number of available DSPs (Digital Signal Processing units) is 220 in the ZC7Z020-CLG484 FPGA device and such configuration requires 202 of these units. Thus, the *DSPs* are the limiting resource of the proposed architecture, because the next possible configuration instantiates 30 *PEs*, so it will demand 257 *DSPs*, i.e. a device with more hardware resources is requested. It is worth mentioning that the number of *PEs* must be a divisor of the number of bands to properly apply the optimizations. Meanwhile, the rest of hardware resources are not critical for the scalability of the architecture, although the BRAMs are between 74% and 83%, it really depends on the block size parameter (*BS*), whose value is set at design time.

The throughput of each configuration of the hardware accelerator is depicted in MSamples per second (MSamples/s), which depends on the number of *PEs* instantiated and the clock frequency configuration. In this sense, the RTL models for the HLS modules were generated setting the target clock frequency at 100MHz. Then, two version of the bitstream were synthesized for two different clock configurations: 100MHz

TABLE II  
HARDWARE UTILIZATION OF HYPERLCA ALGORITHM WITH ADAPTIVE DISTORTION FEATURE FOR A XC7Z020-CLG484 SoC AFTER POST-IMPLEMENTATION PHASE.

PEs	BRAM18K	DSP48E	FlipFlops	LUTs
1	211 (75.36%)	9 (4.09%)	6,146 (5.78%)	7,502 (14.10%)
2	208 (74.29%)	16 (7.27%)	6,186 (5.81%)	8,329 (15.66%)
4	216 (77.14%)	30 (13.64%)	7,048 (6.62%)	9,384 (17.64%)
6	223 (79.64%)	62 (28.18%)	8,134 (7.64%)	10,886 (20.46%)
10	232 (82.86%)	102 (46.36%)	9,684 (9.10%)	12,733 (23.93%)
12	217 (77.50%)	122 (55.45%)	10,573 (9.94%)	14,458 (27.18%)
20	218 (77.86%)	202 (91.82%)	13,834 (13.00%)	19,178 (36.05%)

TABLE III  
MSAMPLES/S ACHIEVED BY THE DIFFERENT VERSIONS OF THE HYPERLCA ACCELERATOR WITH ADAPTIVE DISTORTION FEATURE FOR A XC7Z020-CLG484 SoC.

PEs	1	2	4	6	10	12	20
<b>100 MHz</b>	58	120	236	332	494	562	777
<b>143 MHz</b>	87	180	352	495	734	835	1149

and 143MHz. From previous works, the authors observed that, in some cases, the model generated by the HLS tools differs greatly due to the characteristics of the generation process, resulting in higher scheduling cycles for shorter clock periods. Nevertheless, the Vivado tool was able to handle the better 100MHz RTL generated models and synthesize a valid bitstream for other clock frequencies, fully compliant with the platform timing constraints. Table III lists the average of the MSamples/s achieved by the hardware accelerator according to the number of *PEs* and the configuration of the clock frequency. It is worth mentioning that the MSamples/s metric mainly depends on two configuration parameters of the hardware accelerator: the pattern signature and the rules that determines the compression ratio applied to the current hyperspectral block. Thus, the MSamples/s values of Table III are an average of the results obtained from the four sensed images by the UAV platform by applying three rules, where the fast versions (143MHz) achieve 33% better performance than the slow ones (100MHz).

The hyperspectral sensor used to sense the images is based on a *Specim FX10*, which is a pushbroom camera that can be configured to set the size of each frame and the spatial information sensed, i.e. the block size (*BS*) and the number of hyperspectral bands, respectively. The *BS* has been configured to the maximum allowed by this camera (1024 pixels) because M. Díaz et al. analyze the image quality in [28] by comparing the SNR, RMSE and MAD metrics to determine the quality of the compression process with the same camera, and conclude that the best results are obtained with the maximum block size. Thus, the selected hyperspectral sensor can capture 1024 pixels with 224 bands with a maximum frame rate of 327 FPS (full range) [33], while the frame rate obtained to capture images of 1024 pixels with 180 bands is approximately 400 FPS. Therefore, analyzing the performance results and the features of the hyperspectral camera used to sense the images, the proposed architecture is able to compress hyperspectral information at run-time with 6 *PEs* and the clock frequency configured at

TABLE IV  
POWER CONSUMPTION OF THE DIFFERENT VERSIONS OF THE HYPERLCA ACCELERATOR WITH ADAPTIVE DISTORTION FEATURE FOR A XC7Z020-CLG484 SoC.

PEs		1	2	4	6	10	12	20
100MHz	MSs/W	25	54	106	141	201	232	305
	PL (watts)	0.679	0.648	0.671	0.796	0.893	0.862	0.993
	Temperature (°C)	50.7	50.4	50.6	52.1	53.2	52.8	57.0
143MHz	MSs/W	36	77	149	195	273	316	413
	PL (watts)	0.809	0.759	0.807	0.985	1.131	1.082	1.225
	Temperature (°C)	52.2	51.8	52.2	54.3	55.9	55.4	57.0

143MHz or with 10 *PEs* with the clock frequency set at 100MHz.

From the point of view of energy-efficiency, the number of *PEs* is the factor that increases the power requirements, as well as the working temperature. Table IV lists the energy-efficiency depicted in MSamples/s per watt (MSs/W), i.e. the power consumption obtained by the FPGA-based implementation of the architecture according with the *PEs* and clock frequency parameters, the power-consumption of the hardware accelerator in watts (only the HyperLCA+QoS core) and the working temperature in Celsius grades. The values listed in Table IV have been reported by the AMD-Xilinx for the worst case scenario after post-implementation stage, showing the variation of the different parameters as the SoC configuration increases the number of *PEs*. To do an accurate analysis of the worst-case scenario, the parameters of the process have been set to maximum value in order to obtain the power-consumption and thermal values in such scenario. This way, the power and thermal delivery solution will work with any device that will be shipped [34]. Regarding the energy-efficiency, the MSs/W trade-off has been calculated with the power-consumption including the embedded microcontroller, i.e. the processing system and programmable logic parts of the targeted device. It does not draw a linear behavior since the number of *PEs* working in parallel increases the number of hardware resources, as well as the power-consumption of the FPGA part; the energy budget of the static part is stable. In this sense, Table IV also shows the power utilization by the hardware implementation of the HyperLCA algorithm, which demonstrates that the architecture is highly efficient because the main energy budget is consumed by the hardcoded embedded processor (1.533 watts), so the extra power of the FPGA-based implementation needed is ranging from 0.314 and 0.416 watts for the 100MHz and 143MHz versions, respectively. On top of that, the working temperature does not have a major impact on the 143MHz versions of the system or on the number of *PEs* working in parallel.

Although Vivado's power analysis tools provide accurate power-consumption results after post-implementation phase, there are other hardware components outside the FPGA device that are involved in the compression hyperspectral process, such as external memory (RAM), that are not considered in the power reports. Unfortunately, the ZedBoard platform,

TABLE V  
POWER CONSUMPTION OF THE DESIGN ON ZEDBOARD  
(XC7Z020-CLG484) WITH CURRENT SENSE (J21 CONNECTOR).

PEs		1	2	4	6	10	12	20
100MHz	Watts	3.624	3.612	3.636	3.642	3.654	3.660	3.720
	MSs/W	16	33	64	91	135	153	208
143MHz	Watts	3.660	3.648	3.660	3.696	3.714	3.720	3.768
	MSs/W	23	49	96	133	197	224	304

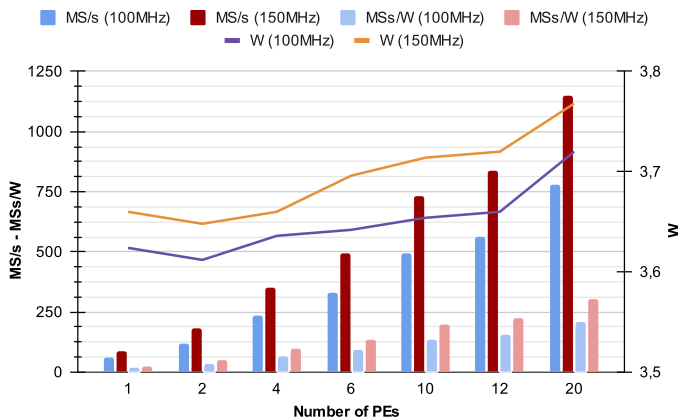


Fig. 7. Performance and power trade-off analysis of HyperLCA algorithm with adaptive distortion feature in its versions 100MHz and 143MHz on ZedBoard (XC7Z020-CLG484) through the current sense (J21 connector).

which includes XC7Z020-CLG484 as programmable logic part, does not have multiple power sources to obtain real-time information about the power consumption, so a fine-grain measurement cannot be performed such as AMD-Xilinx power estimation tool does. On the other hand, the Vivado hardware manager tool monitors the supply voltage of Processing System (PS) and Programmable Logic (PL) parts, but the refresh rate is too low. Therefore, the power-consumption of the architecture presented in this paper has been measured in the ZedBoard platform across the on-board current sense port (J21 connector), using a multimeter with enough resolution to show the difference in power-consumption when a compression process is performed [35]. Table V lists the power-consumption in watts and energy-efficiency in MSamples/s per watt (MSs/W) in the different versions of the HyperLCA with distortion feature. To calculate the current power-consumption, the multimeter has been connected to the J21 connector to measure the voltage across a  $10m\Omega$  resistor. Thus, the power input to the board is calculated with the following equations, where  $V_{j21}$  is the voltage measured in the J21 connector,  $R$  is  $10m\Omega$  and  $V_{in}$  is the input supply voltage ( $V_{in} = 12V$ ).

$$I = V_{j21}/R \quad (10)$$

$$P(\text{watts}) = I * V_{in} \quad (11)$$

Figure 7 graphically shows a comparison of performance and power-consumption trade-off between the 100MHz (blue

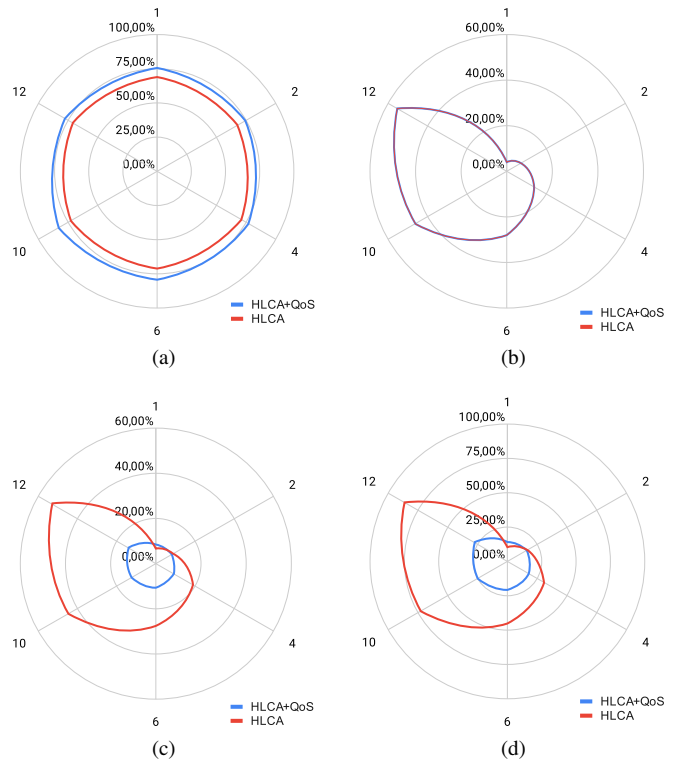


Fig. 8. Comparison of hardware resource utilization in HyperLCA algorithm with and without adaptive distortion feature. (a) BRAM18K. (b) DSP48E. (c) FlipFlops. (d) LUTs.

bars and purple line) and 143MHz (red bars and orange line) of HyperLCA algorithm with adaptive distortion feature. The power-consumption has the similar behavior in both versions, whose variations depends on the number of  $PEs$  working in parallel, whilst energy efficiency in the 143MHz version is 30% higher than 100MHz version. On the other hand, the efficiency variation with respect to the data collected in Table IV, where only the FPGA power consumption (PS + PL) is taken into account, it has been reduced by 35% and 31% for the 100MHz and 143MHz versions, respectively.

## V. DISCUSSION

The HyperLCA algorithm with adaptive distortion feature has been compared with the previous implementation published in [8]. Both hyperspectral lossy compressors have been implemented on reconfigurable hardware, concretely in a ZC7Z020-CLG484 FPGA device. Thus, the performance and hardware resource utilization of the two versions are compared and analyzed, as well as the information extracted by each implementation in terms of size and quality. In addition, the hyperspectral lossy compressor presented in this manuscript has been compared with other state-of-the-art transform-based compressors, in which reconfigurable devices have been selected to deal with the experimental results of the proposals.

### A. Comparison with the previous hardware implementation of the HyperLCA lossy compressor

Figure 8 graphically shows the hardware resource utilization of the HyperLCA algorithm with (HLCA+QoS) and without

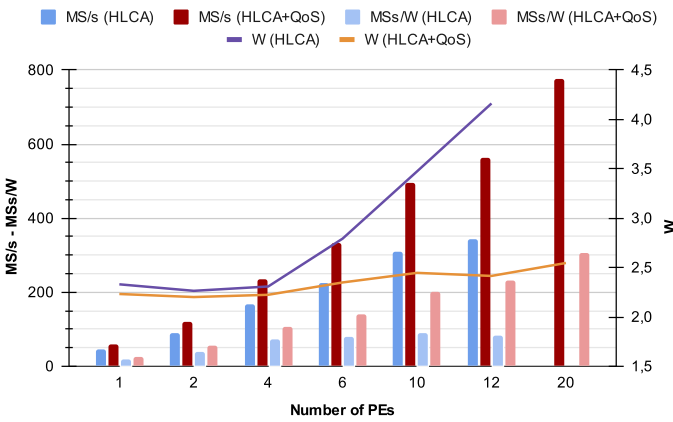


Fig. 9. Performance and power trade-off analysis of HyperLCA algorithm with and without adaptive distortion feature (100MHz).

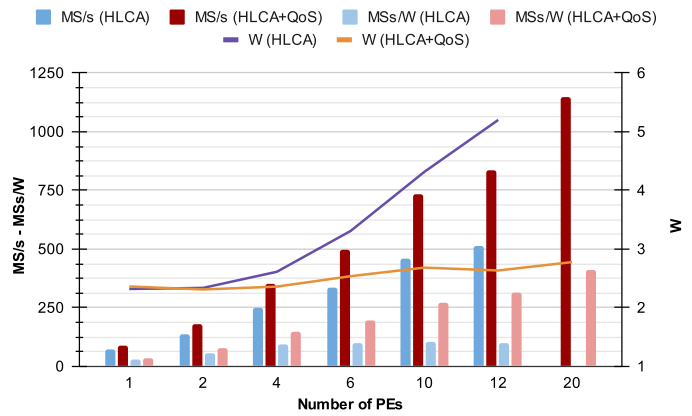


Fig. 10. Performance and power trade-off analysis of HyperLCA algorithm with and without adaptive distortion feature (143MHz).

(HLCA) adaptive distortion feature. The number of BRAMs increases slightly in this new version of the algorithm because the pattern analysis stage introduces new internal memories (see Figure 8a), while the number of DSPs is kept (see Figure 8b). However, FlipFlops and LUTs are considerably reduced by some optimizations performed; the main optimization carried out is the manual partitioning of the orthogonal vectors,  $\mathbf{u}$  and  $\mathbf{q}$ , by a factor equal to the number of PEs that contains the hardware accelerator. For the sake of clarity, the FFs and LUTs are the limiting factor that prevents the deployment of PEs in the previous version of the hardware accelerator, rather than DSPs which are the limiting factor in this new version. Thus, the best configuration of the HyperLCA with distortion feature, i.e. the 20 PEs version is not considered in the hardware resource utilization comparison because it cannot be compared.

The performance and power trade-off achieved by the HyperLCA with and without adaptive distortion feature are shown in Figure 9 and 10, where the clock frequency has been configured at 100MHz and 143MHz, respectively. The new version gets better MSamples/s per watt (MSs/W), it is doubled in the configurations that instantiate 10 and 12 PEs; the light blue bars of Figure 9 and 10 show the MSs/W achieved by the previous implementation of the HyperLCA, whilst the light red bars of the aforementioned figures represent the obtained MSs/W by the implementation presented in this manuscript. The other configurations slightly improve the MSamples/s achieved (see blue and red bars of Figure 9 and 10). In turn, the performed optimizations also reduce the power consumption of the hardware accelerator respect to the previous version, which is more evident for cases with a higher number of instantiated PEs; purple and orange lines of Figure 9 and 10 draw the watts of the hardware accelerator with and without adaptive distortion feature, respectively.

The previous implementation of the hyperspectral lossy compressor extracts the identical amount of spectral information from each block that compose the hyperspectral image, so the applied compression ratio is linear and is defined at design time. It means the size of extracted data is equal for hyperspectral images with the same spatial and spectral values and the quality performance of compression is kept. Nevertheless, the

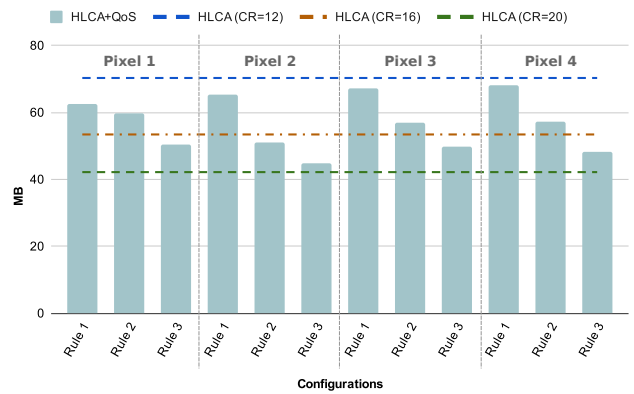


Fig. 11. Compression data size of HyperLCA algorithm with and without adaptive distortion feature with different configurations.

adaptive distortion feature introduces a non-linear behavior in terms of quality performance and compression ratio, as well as preserves the linearity feature of transform-based algorithms, i.e. the set of core operations applied to extract the spectral information has a linear behavior. To do so, the number of iterations performed on the set of core operations is set by the pre-defined rules which depends on the number of pixels close to the hyperspectral pattern signature. For experimental results, the three rules, listed in Table VI, have been defined to be applied on the sensed images, meanwhile the pattern signatures have been selected from a previous flight, in where the weather was similar to that of the compression flight.

Figure 11 graphically shows the compression data size after the compression process of a hyperspectral image of 377.5MB using the previous implementation of the HyperLCA algorithm and the modified one. The hyperspectral cube is composed by 1024 samples, 1024 lines and 180 bands. The compression ratio of the original implementation of the HyperLCA lossy compressor has been set at design time with the following values  $CR = 12$ ,  $CR = 16$  and  $CR = 20$ , which match with blue, orange and green dotted lines of Figure 11, respectively. On the other hand, the blue bars of Figure 11 illustrate the non-linear behavior of the spectral extraction in the HyperLCA lossy compressor with adaptive distortion, in which four hyperspectral pixels have been selected as signature patterns to



TABLE VI  
DEFINED RULES FOR EXPERIMENTAL RESULTS PURPOSE.

$N_{iter}$	$Q_{max}$ (12)	$Q_{min}$ (7)	$Q_{med}$ (9)
<b>Rule 1</b>	$T_c \geq 100$	$T_c \leq 50$	otherwise
<b>Rule 2</b>	$T_c \geq 800$	$T_c \leq 200$	otherwise
<b>Rule 3</b>	$T_c \geq 800$	$T_c \leq 600$	otherwise

obtain the number of iterations to be applied for each sample of the image according to the rules defined in Table VI. The number of iterations ( $N_{iter}$ ) have been set to 12, 9 and 7 for the high, medium and low quality of service, respectively. These values match with the number of iterations performed by the original implementation of the HyperLCA algorithm in the three aforementioned  $CR$  configurations, but it can be modified to obtain better compression quality performance.

It is worth mentioning that each hyperspectral block,  $\mathbf{M}_k$ , contains a header block (see Figure 4), so a small size overhead is included. This overhead is actually 8 bits per block, i.e. 1KB is the overhead introduced by the proposed solution for the images used because they contain 1024 lines. Therefore, the maximum and minimum size of the compressed data are close to blue and green dotted lines of Figure 11. Since the compression size depends on the two aforementioned factors.

The compression performance of the HyperLCA with adaptive distortion has been evaluated by compressing/decompressing a hyperspectral image with four pattern signatures and three rules (see Table VI). The spectral information lost after the compression process has been analyzed using three conventional metrics: the *Signal-to-Noise Ratio (SNR)*, the *Root Mean Squared Error (RMSE)* and the *Maximum Absolute Difference (MAD)*, which are shown in Equations (12)–(14), respectively. The *SNR* and the *RMSE* provides the average information lost in the compression process, where high values of the *SNR* metric are signs of better compression performance. Meanwhile higher *RMSE* values mean the compression process is not accurate and introduces large information losses. Finally, the *MAD* metric depicts the amount of lost information for the worst reconstructed image value, where 4096 ( $2^{12}$ ) is the worst possible value.

$$SNR = 10 \cdot \log_{10} \left( \frac{\sum_{i=1}^{nb} \sum_{j=1}^{np} (I_{i,j})^2}{\sum_{i=1}^{nb} \sum_{j=1}^{np} (I_{i,j} - Ic_{i,j})^2} \right) \quad (12)$$

$$RMSE = \frac{1}{np \cdot nb} \cdot \sqrt{\sum_{i=1}^{nb} \sum_{j=1}^{np} (I_{i,j} - Ic_{i,j})^2} \quad (13)$$

$$MAD = \max(I_{i,j} - Ic_{i,j}) \quad (14)$$

Table VII shows the average results obtained for the HyperLCA compressor in the three first rows for  $CR = 12$ ,  $CR = 16$  and  $CR = 20$ , whilst the rest of rows are the result obtained by the modified version of the algorithm, i.e. including the adaptive distortion feature. These results draw different conclusions that should be considered. Firstly, the

TABLE VII  
COMPARISON OF THE QUALITY COMPRESSION RESULTS FOR THE HYPERLCA WITH AND WITHOUT ADAPTIVE DISTORTION FEATURE.

Version	Configuration	SNR	MAD	MSE	
HLCA	$N_{bits} = 12$	$CR = 12$	43.01	24.50	3.12
		$CR = 16$	42.27	34.25	3.40
		$CR = 20$	41.31	41.25	3.73
HLCA+QoS	Pixel 1	Rule 1	42.54	29.07	3.29
		Rule 2	41.83	36.16	3.54
		Rule 3	41.31	41.25	3.73
	Pixel 2	Rule 1	42.72	27.40	3.22
		Rule 2	41.49	39.51	3.67
		Rule 3	41.88	35.71	3.53
	Pixel 3	Rule 1	42.85	26.11	3.18
		Rule 2	42.21	32.42	3.41
		Rule 3	41.71	37.39	3.59
	Pixel 4	Rule 1	42.89	25.72	3.16
		Rule 2	42.26	31.97	3.39
		Rule 3	41.71	37.39	3.59

results are between the lowest and highest configurations of the original implementation because the QoS has been defined with the same number of iterations that the configuration set for the implementation without distortion feature. In addition, it is confirmed that the proposed solution provides better-quality compression results than the ones obtained by the previous implementation with the highest compression ratio. It is worth mentioning that the compression performance results obtained by the *Pixel 1 - Rule 1* configuration are equal to the  $CR = 20$  configuration, but the spectral information extracted differs because the distortion feature is able to retrieve more spectral information from the areas of interest, hence the data compression size is larger (see Figure 11). Furthermore, it can be also concluded that the HyperLCA lossy compressor with adaptive distortion is able to compress the hyperspectral data with high compression ratios and without introducing significant spectral information losses.

### B. Comparison with other state-of-the-art compressors

Furthermore, the throughput and hardware resource utilization of the hyperspectral lossy compressor with adaptive distortion feature have been compared with other state-of-the-art compressors also implemented on reconfigurable hardware. The state-of-the-art architectures and the one explained in this manuscript are summarized in Table VIII, where the selected device, the implemented algorithm, the hardware resource utilization, the clock frequency and the achieved throughput (MSamples/s) are listed for each proposal. In addition, the performance analysis has been expanded in Table IX, where the power consumption is included, as well as the relationship between throughput in MB/s and watts.

Prediction-based compression algorithms are good candidates to be implemented on reconfigurable hardware because of the suitability of matrix operations on them. Typically, they depend on the correlation between adjacent pixels in

TABLE VIII  
HARDWARE RESOURCE AND THROUGHPUT COMPARISON WITH OTHER FPGA-BASED IMPLEMENTATIONS OF HYPERSPECTRAL COMPRESSORS.

Proposal	Device	Programming Method	Compression Algorithm	BRAMs	DSPs	FFs	LUTs	Freq. (MHz)	Throughput (MSamples/s)
L. Santos et al.[36]	XQR5VFX130	HLS	LCE	17 (02.85%)	4 (01.25%)	4,208 (20.55%)	7,836 (05.98%)	80.2	30.25
A. García et al.[37]	XC5VFX100	HLS	LCE	4 (00.88%)	25 (09.77%)	1,937 (03.03%)	7,746 (12.10%)	86.96	27.7
D. Keymulen (1 core)[38]	XC7VX690T	VHDL	FLEX (CCSDS)	72 (02.45%)	31 (00.86%)	9,158 (01.06%)	13,134 (03.03%)	200	9
D. Keymulen (15 cores)[38]	XC7VX690T	VHDL	FLEX (CCSDS)	1,112 (37.82%)	465 (12.92%)	260,750 (30.10%)	297,807 (34.37%)	100	95
D. Fernández et al.[39]	XC7VFX690T	VHDL	PCA	897 (30.51%)	2,580 (71.67%)	57,564 (06.64%)	294,454 (67.99%)	75.99	80.29
D. Báscones et al.[40]	XQR5VFX130	VHDL	LCPLC-JYPEC	10 (01.68%)	5 (01.56%)	-	6,837 (05.22%)	247.35	119.96
D. Báscones et al.[41]	XC7VX690T	VHDL	LCPLC-JYPEC	6 (00.20%)	5 (00.14%)	-	6,731 (01.55%)	341.99	162.3
Y. Barrios et al. (1 core) [42]	XCZU9EG	HLS	CCSDS	39 (04.28%)	5 (00.20%)	8,639 (01.58%)	11,965 (04.37%)	100	0.4
Y. Barrios et al. (8 cores)[42]	XCZU9EG	HLS	CCSDS	312 (34.21%)	26 (01.03%)	42,771 (07.80%)	56,800 (20.72%)	100	1.7
J. Caba et al. (12 PEs) [8]	ZC7Z020	VHDL-HLS	HyperLCA	199 (71.07%)	122 (55.45%)	56,463 (53.07%)	46,116 (86.68%)	100	342
J. Caba et al. (12 PEs) [8]	ZC7Z020	VHDL-HLS	HyperLCA	199 (71.07%)	122 (55.45%)	56,463 (53.07%)	46,116 (86.68%)	143	511
Our (20 PEs)	ZC7Z020	VHDL-HLS	HyperLCA	218 (77.86%)	202 (91.82%)	20,028 (18.82%)	19,415 (36.49%)	100	777
Our (20 PEs)	ZC7Z020	VHDL-HLS	HyperLCA	218 (77.86%)	202 (91.82%)	20,028 (18.82%)	19,415 (36.49%)	143	1,149

hyperspectral data, in which the differences between correlated values are encoded with fewer bits than the actual values. D. Báscones et al. present an architecture based on Low Complexity Predictive Lossy Compression (LCPLC), which is an algorithm based on prediction, uniform threshold quantization, and rate-distortion optimization. Thus, the proposed solution implements a pipeline architecture developed in VHDL and deployed on XQR5VFX130 and XC7VX690T devices in [40] and [41], respectively. The proposed architecture achieves a throughput up to 162 MSamples/s and a low power requirement, roughly 0.714 watts. Meanwhile, LCE (Lossy Compression for Exomars) is an algorithm designed for on-board image compression for the European Space Agency (ESA) ExoMars mission. It consists of four phases: prediction, rate-distortion optimization, quantization, and entropy coding using Golomb codes. It has been accelerated by L. Santos et al. and A. García et al. in [36] and [37] using reconfigurable hardware. Both solutions have been developed with HLS (CatapultC), by obtaining good ratio between hardware utilization and throughput. D. Keymulen implements the FLEX algorithm by introducing a feedback branch with an inverse predictor in [38]. It can estimate the value of subsequent samples by controlling the image quality with an adaptive filtering defined by the user. The architecture achieves up to 95 MSamples/s when 15 cores are instantiated by increasing  $19\times$  when only one core is working, however the hardware utilization is considerably increased.

Y. Barrios et al. propose in [42] the implementation of a lossy extension of CCSDS by adding a quantizer and a bit-rate feedback loop, to control the losses and achieve the desired compression ratios without excessively deteriorating the quality of the decompressed image. The algorithm has been implemented using HLS techniques, and has been implemented on a reconfigurable, scalable architecture (ARTICo), which provides adaptive computing at run-time to increase the number of instantiated cores and, hence, the performance achieved. Thus, the solution working with one core gets 0.4 MSamples/s, whilst the one instantiating 8 cores achieves 1.7 MSamples/s. Although the run-time flexibility of the ARTICo architecture is a value-added feature in space scenarios, the main problem lies in the context switches and in the movement of data to the local memories of each of the eight reconfigurable regions.

The transform-based algorithms are also suitable on reconfigurable hardware. The basic idea behind this class of algorithms is to map the spatial domain of an image into its transformation domain. Then, the coefficients with larger amplitude, or energy, are encoded with fewer codewords than coefficients with low amplitude to obtain higher compression ratios. The transform function is first applied to generate the transform coefficients. Then, the transform coefficients are decorrelated to remove redundancy. Finally, the output coefficients are passed to the entropy encoder to generate the compressed stream. D. Fernández et al. propose in [39] a PCA-based (Principal Component Analysis) solution in reconfigurable hardware by using VHDL to carry out the dimensionality reduction in hyperspectral images. Meanwhile, the architecture presented in this manuscript and its previous implementation in [8] are based on transform operations, in which a high parallelization of the operations results in the highest performance.

From the point of view of hardware resource utilization, Table VIII lists the FPGA-based resource utilization of each hyperspectral compressor and its percentage according to the selected device. Thus, the percentage of utilization can be used to compare the state-of-the-art architectures in order to avoid misleading interpretations of information, where most solution use mid or large FPGA devices instead of cost-optimized ones, or where customized embedded resources, such as DSPs, are not properly used to perform mathematical operations. In this sense, our architecture achieves the best throughput of the proposed architectures, up to 1,149 MSamples/s, it is mainly due to the instantiation of DSPs to carry out the operations of transformations instead of the use other unsuitable FPGA resources for such operations. This behavior is also seen in other proposals, such as the one presented by D. Fernández et al. in [39] or D. Keymulen in [38]; the version with 15 cores working in parallel presented by D. Keymulen achieves higher throughput than the version with a core; it increases the number of DSPs and reduces the clock frequency. It can be concluded that the use of a hybrid solution, VHDL and HLS, obtains a good use of hardware resources and maintains the benefits of both, i.e. the engineer productivity is kept by using HLS to describe some modules/parts of the architecture, whilst the modules that require a high degree of parallelism are developed with a hardware description language (HDL),

TABLE IX  
PERFORMANCE COMPARISON WITH OTHER FPGA-BASED IMPLEMENTATIONS OF HYPERSPECTRAL COMPRESSORS.

Proposal	Hyperspectral Image	Samples	Lines	Bands	Throughput (MSamples/s)	MB/s	Watts	MBS/W
L. Santos et al.[36]	-	16	16	256	30.25	0.236	2.029*	0.116
A. García et al.[37]	AVIRIS (Jasper Ridge)	614	512	224	27.7	5.449	2.022*	2.695
D. Keymulen (1 core)[38]	AVIRIS (Jasper Ridge)	614	512	224	9	4.722	7.84	0.602
D. Keymulen (15 cores)[38]	AVIRIS (Jasper Ridge)	614	512	224	95	49.842	11.4	4.372
D. Fernández et al.[39]	AVIRIS (Jasper Ridge)	614	512	224	80.29	9.004	2.46*	3.661
D. Báscones et al.[40]	AVIRIS	512	512	256	119.96	29.99	2.732	10.977
D. Báscones et al.[41]	AVIRIS	512	512	256	162.3	40.575	0.714	56.828
Y. Barrios et al. (1 core) [42]	AVIRIS	512	512	256	0.4	0.1	0.6*	0.167
Y. Barrios et al. (8 cores)[42]	AVIRIS	512	512	256	1.7	0.425	0.9*	0.472
J. Caba et al. (12 PEs) [8]	Own ( <i>Specim FX10</i> )	1024	1024	180	342	120.234	1.6	75.146
J. Caba et al. (12 PEs) [8]	Own ( <i>Specim FX10</i> )	1024	1024	180	511	179.648	2.22	80.923
Our (20 PEs - 100MHz)	Own ( <i>Specim FX10</i> )	1024	1024	180	777	273.164	0.993	275.089
Our (20 PEs - 143MHz)	Own ( <i>Specim FX10</i> )	1024	1024	180	1,149	403.945	1.225	329.751

\*Obtained from Xilinx Power Estimator datasheet (XPE).

as well as the FSM to synchronize the parts described with HLS.

Table IX shows a detailed performance summary achieved by the state-of-the-art architectures and the one presented in this work, using the values obtained after post-implementation phase in order to analyze the architectures at the same point. In addition, the table also lists in the second last column the on-chip power depicted in watts. Unfortunately, some state-of-the-art proposals do not provide such information, so it has been estimated with the Xilinx Power Estimator tool (XPE). The use of specialized embedded resources of the FPGA does not have a high impact in the power consumption, but it depends on the number of clock regions that are active, the amount of resources and the FPGA technology used. In this sense, the architecture presented by D. Keymulen in [38] requires more power than the one presented by D. Báscones et al. in [41], where both proposals use the same FPGA device and VHDL to describe the architecture; the difference lies in the number of FPGA resources used for each proposal. We can conclude that the architecture presented in this work beats the other state-of-the-art proposals in the MB/s per Watt (MBS/W) trade-off, where the fastest version of the HyperLCA compressor with distortion feature, i.e. the version that contains 20 PEs working in parallel, is between  $4.9\times$  and  $5.8\times$  better than the architecture presented by D. Báscones et al. in [41], when the clock frequency is configured at 100MHz and 143MHz, respectively.

It is worth mentioning that the previous implementation of the HyperLCA compressor is between  $3.6\times$  and  $4.1\times$  slower than the version with adaptive distortion feature. In addition, the clock frequency configuration has little influence on the rate of MB/s per watt, it is increased 54.66 MBS/W when the clock frequency is set to 143MHz. Therefore, the architecture presented in this work is able to compress the aforementioned hyperspectral image of 1024x1024 spatial size and 180 spectral bands in 0.935s with a power consumption of 1.145W.

## VI. CONCLUSION

This work has dealt with the inclusion of the adaptive distortion feature in the HyperLCA algorithm in order to increase the spectral information in those regions of interest, whose spectral information contains an amount of pixels close

to a predefined hyperspectral pattern signature. Thus, the proposal can be adapted to the scenario that is being processed, e.g., more spectral information could be collected from the vegetation than from the soil in a vineyard. In addition, the compressor can be configured to increase the information in the lines which contain anomaly pixels, e.g. ships in the middle of the sea.

The set of core hyperspectral operations is inherited from previous works [8], [9] where the suitability of the FPGA technology for this type of applications was tested, so a significant amount of time is saved. However, the new architecture includes new optimizations that allows to instantiate more PEs working in parallel. Consequently, the throughput is considerably increased by the optimizations performed, whereas the adaptive distortion feature introduces a small overhead in size terms due to the need to include an 8-bit header for each sample that is compressed. The solution combines HLS and VHDL modules, bringing an efficient dataflow that meets the requirements of an on-board real-time processing with a pushbroom camera, concretely with the *Specim FX10*.

Furthermore, we provide a comparison with other FPGA-based architectures of the state-of-the-art, in which the conclusions learned from the discussion reveal that the proposed architecture is a cost-energy efficient solution without reducing the compression quality, when the number of transform-based operations carried out is between the ones defined in the previous implementation. Moreover, the loss spectral information can be reduced by increasing the parameter  $p_{max}$ , so better compression quality can be achieved.

## ACKNOWLEDGMENT

This research has been funded by H2020 European Union program under grant agreement No. 857159 (SHAPES project) and by the Ministry of Economy and Competitiveness (MINECO) of the Spanish Government under TALENT project (PID2020-116417RB-C4, subprojects 1 and 4) and MIRATAR project (TED2021-132149B-C41).

## REFERENCES

- [1] A. Plaza, J. A. Benediktsson, J. W. Boardman, J. Brazile, L. Bruzzone, G. Camps-Valls, J. Chanussot, M. Fauvel, P. Gamba, A. Gualtieri *et al.*, "Recent advances in techniques for hyperspectral image processing," *Remote sensing of environment*, vol. 113, pp. S110–S122, 2009.

- [2] A. Altamimi and B. Ben Youssef, "A systematic review of hardware-accelerated compression of remotely sensed hyperspectral images," *Sensors*, vol. 22, no. 1, 2022.
- [3] M. Radosavljević, B. Brkljač, P. Lugonja, V. Crnojević, Ž. Trpovski, Z. Xiong, and D. Vukobratović, "Lossy compression of multispectral satellite images with application to crop thematic mapping: A hev comparative study," *Remote Sensing*, vol. 12, no. 10, p. 1590, 2020.
- [4] F. Ortenberg, P. Thenkabail, J. Lyon, and A. Huete, "Hyperspectral sensor characteristics: airborne, spaceborne, hand-held, and truck-mounted; integration of hyperspectral data with lidar," *Hyperspectral Remote sensing of vegetation*, pp. 39–68, 2011.
- [5] J. M. Melián, A. Jiménez, M. Díaz, A. Morales, P. Horstrand, R. Guerra, S. López, and J. F. López, "Real-Time Hyperspectral Data Transmission for UAV-Based Acquisition Platforms," *Remote Sensing*, vol. 13, no. 5, 2021.
- [6] E. Morin, M. Maman, R. Guizzetti, and A. Duda, "Comparison of the Device Lifetime in Wireless Networks for the Internet of Things," *IEEE Access*, vol. 5, pp. 7097–7114, 2017.
- [7] R. Guerra, E. Martel, J. Khan, S. López, P. Athanas, and R. Sarmiento, "On the Evaluation of Different High-Performance Computing Platforms for Hyperspectral Imaging: An OpenCL-Based Approach," *IEEE Journal of Selected Topics in Applied Earth Observations and Remote Sensing*, vol. 10, no. 11, pp. 4879–4897, 2017.
- [8] J. Caba, M. Díaz, J. Barba, R. Guerra, and J. A. d. I. T. a. López, "FPGA-Based On-Board Hyperspectral Imaging Compression: Benchmarking Performance and Energy Efficiency against GPU Implementations," *Remote Sensing*, vol. 12, no. 22, 2020. [Online]. Available: <https://www.mdpi.com/2072-4292/12/22/3741>
- [9] R. Guerra, Y. Barrios, M. Díaz, A. Baez, S. López, and R. Sarmiento, "A hardware-friendly hyperspectral lossy compressor for next-generation space-grade field programmable gate arrays," *IEEE Journal of Selected Topics in Applied Earth Observations and Remote Sensing*, vol. 12, no. 12, pp. 4813–4828, 2019.
- [10] G. Benelli, G. Meoni, and L. Fanucci, "A low power keyword spotting algorithm for memory constrained embedded systems," in *2018 IFIP/IEEE International Conference on Very Large Scale Integration (VLSI-SoC)*, 2018, pp. 267–272.
- [11] T. Yan, N. Zhang, J. Li, W. Liu, and H. Chen, "Automatic Deployment of Convolutional Neural Networks on FPGA for Spaceborne Remote Sensing Application," *Remote Sensing*, vol. 14, no. 13, 2022.
- [12] M. Xu, L. Chen, H. Shi, Z. Yang, J. Li, and T. Long, "FPGA-Based Implementation of Ship Detection for Satellite On-Board Processing," *IEEE Journal of Selected Topics in Applied Earth Observations and Remote Sensing*, vol. 15, pp. 9733–9745, 2022.
- [13] S. Liu and W. Luk, "Towards an Efficient Accelerator for DNN-Based Remote Sensing Image Segmentation on FPGAs," in *2019 29th International Conference on Field Programmable Logic and Applications (FPL)*, 2019, pp. 187–193.
- [14] G. Furano, G. Meoni, A. Dunne, D. Moloney, V. Ferlet-Cavrois, A. Tavoularis, J. Byrne, L. Buckley, M. Psarakis, K.-O. Voss, and L. Fanucci, "Towards the use of artificial intelligence on the edge in space systems: Challenges and opportunities," *IEEE Aerospace and Electronic Systems Magazine*, vol. 35, no. 12, pp. 44–56, 2020.
- [15] L. Li, S. Zhang, and J. Wu, "Efficient object detection framework and hardware architecture for remote sensing images," *Remote Sensing*, vol. 11, no. 20, 2019.
- [16] Intel Movidius, "VPU Intel Movidius Myriad X," Available Online: <https://www.intel.es/content/www/es/es/products/sku/204770/intel-movidius-myriad-x-vision-processing-unit-0gb/specifications.html>, (Accessed on 10 March 2023).
- [17] Coral.ai, "Coral dev board datasheet," Available Online: <https://coral.ai/docs/dev-board/datasheet/#system-components>, (Accessed on 10 March 2023).
- [18] V. Kothari, E. Liberis, and N. D. Lane, "The Final Frontier: Deep Learning in Space," in *Proceedings of the 21st International Workshop on Mobile Computing Systems and Applications*, ser. HotMobile '20. New York, NY, USA: Association for Computing Machinery, 2020, p. 45–49.
- [19] E. Rapuano, G. Meoni, T. Pacini, G. Dinelli, G. Furano, G. Giuffrida, and L. Fanucci, "An fpga-based hardware accelerator for cnns inference on board satellites: Benchmarking with myriad 2-based solution for the cloudscout case study," *Remote Sensing*, vol. 13, no. 8, 2021.
- [20] B. Huang, *Satellite data compression*. Springer Science & Business Media, 2011.
- [21] Consultative Committee for Space Data Systems (CCSDS), "Image Data Compression. CCSDS, Green Book 120.1-G-3." Available Online: <https://public.ccsds.org/Pubs/120x1g3.pdf>, (Accessed on 29 September 2022).
- [22] Y. Dua, V. Kumar, and R. S. Singh, "Comprehensive review of hyper-spectral image compression algorithms," *Optical Engineering*, vol. 59, no. 9, pp. 1 – 39, 2020.
- [23] A. B. Kiely, M. Klimesh, I. Blanes, J. Ligo, E. Magli, N. Aranki, M. Burl, R. Camarero, M. Cheng, S. Dolinar *et al.*, "The new ccsds standard for low-complexity lossless and near-lossless multispectral and hyperspectral image compression," 2018.
- [24] E. Augé, J. E. Sánchez, A. B. Kiely, I. Blanes, and J. Serra-Sagrasta, "Performance impact of parameter tuning on the CCSDS-123 lossless multi-and hyperspectral image compression standard," *Journal of Applied Remote Sensing*, vol. 7, no. 1, p. 074594, 2013.
- [25] L. Santos, E. Magli, R. Vitulli, J. F. López, and R. Sarmiento, "Highly-parallel GPU architecture for lossy hyperspectral image compression," *IEEE Journal of Selected Topics in Applied Earth Observations and Remote Sensing*, vol. 6, no. 2, pp. 670–681, 2013.
- [26] Y. Barrios, A. J. Sánchez, L. Santos, and R. Sarmiento, "SHyLoC 2.0: A Versatile Hardware Solution for On-Board Data and Hyperspectral Image Compression on Future Space Missions," *Ieee Access*, vol. 8, pp. 54 269–54 287, 2020.
- [27] R. Guerra, Y. Barrios, M. Díaz, L. Santos, S. López, and R. Sarmiento, "A new algorithm for the on-board compression of hyperspectral images," *Remote Sensing*, vol. 10, no. 3, p. 428, 2018.
- [28] M. Díaz, R. Guerra, P. Horstrand, E. Martel, S. López, J. F. López, and S. Roberto, "Real-Time Hyperspectral Image Compression Onto Embedded GPUs," *IEEE Journal of Selected Topics in Applied Earth Observations and Remote Sensing*, pp. 1–18, 2019.
- [29] I. Vasilyeva, F. Li, S. Abramov, V. V. Lukin, B. Vozel, and K. Chehdi, "Lossy compression of three-channel remote sensing images with controllable quality," in *Image and Signal Processing for Remote Sensing XXVII*, L. Bruzzone and F. Bovolo, Eds., vol. 11862, International Society for Optics and Photonics. SPIE, 2021, pp. 205 – 216.
- [30] P. G. Howard and J. S. Vitter, "Fast and efficient lossless image compression," in *Data Compression Conference, 1993. DCC'93*. IEEE, 1993, pp. 351–360.
- [31] J. Cong, B. Liu, S. Neuendorffer, J. Noguera, K. Vissers, and Z. Zhang, "High-Level Synthesis for FPGAs: From Prototyping to Deployment," *IEEE Transactions on Computer-Aided Design of Integrated Circuits and Systems*, vol. 30, no. 4, pp. 473–491, April 2011.
- [32] P. Horstrand, R. Guerra, A. Rodríguez, M. Díaz, S. López, and J. F. López, "A UAV platform based on a hyperspectral sensor for image capturing and on-board processing," *IEEE Access*, vol. 7, pp. 66 919–66 938, 2019.
- [33] Specim, Spectral Imaging Ltd, "Specim fx10 datasheet," Available Online: <https://www.specim.fi/wp-content/uploads/2020/02/Specim-FX10-Technical-Datasheet-04.pdf>, (Accessed on 1 December 2022).
- [34] AMD-Xilinx, "Seven Steps to an Accurate Worst-Case Power Analysis using the Xilinx Power Estimator," Available Online: <https://docs.xilinx.com/v/u/en-US/xapp1348-power-analysis>, (Accessed on 15 April 2023).
- [35] Velleman, "User Manual: DVM1200 - Multimeter with USB interface," Available Online: <https://www.velleman.eu/downloads/1/dvm1200gbnlfresdplit.pdf>, (Accessed on 26 May 2023).
- [36] L. Santos, J. F. López, R. Sarmiento, and R. Vitulli, "FPGA implementation of a lossy compression algorithm for hyperspectral images with a high-level synthesis tool," in *2013 NASA/ESA Conference on Adaptive Hardware and Systems (AHS-2013)*, 2013, pp. 107–114.
- [37] A. García, L. Santos, S. López, G. Marrero, J. F. López, and R. Sarmiento, "High level modular implementation of a lossy hyperspectral image compression algorithm on a FPGA," in *2013 5th Workshop on Hyperspectral Image and Signal Processing: Evolution in Remote Sensing (WHISPERS)*, 2013, pp. 1–4.
- [38] D. Keymeulen, "FPGA implementation of lossless and lossy compression of space-based multispectral and hyperspectral imagery," 2016.
- [39] D. Fernández, C. González, D. Mozos, and S. Lopez, "FPGA implementation of the principal component analysis algorithm for dimensionality reduction of hyperspectral images," *Journal of Real-Time Image Processing*, vol. 16, 2019.
- [40] D. Báscones, C. González, and D. Mozos, "An Extremely Pipelined FPGA Implementation of a Lossy Hyperspectral Image Compression Algorithm," *IEEE Transactions on Geoscience and Remote Sensing*, vol. 58, no. 10, pp. 7435–7447, 2020.
- [41] —, "An FPGA Accelerator for Real-Time Lossy Compression of Hyperspectral Images," *Remote Sensing*, vol. 12, no. 16, 2020.
- [42] Y. Barrios, A. Rodríguez, A. Sánchez, A. Pérez, S. López, A. Otero, E. de la Torre, and R. Sarmiento, "Lossy Hyperspectral Image Compression on a Reconfigurable and Fault-Tolerant FPGA-Based Adaptive Computing Platform," *Electronics*, vol. 9, no. 10, 2020.





**Julián Caba** received the M.S. degree in Computer Science and the Ph.D. from the University of Castilla-La Mancha (UCLM), Spain, in 2009 and 2018, respectively. He won the Ph.D. category in the Xilinx Open Hardware Contest in 2017. He is currently an Assistant Professor with the TSI Department, UCLM. His current research interests include hardware verification methodologies, embedded systems, high-level synthesis, run-time reconfigurable systems and heterogeneous distributed systems.



**Fernando Rincón** received the degree in computer science from the Autonomous University of Barcelona, Barcelona, Spain, in 1993, and the Ph.D. degree from the University of Castilla-La Mancha, Ciudad Real, Spain. He is currently an Assistant Professor with the TSI Department, University of Castilla-La Mancha. His research interests include system-on-chip integration, HW run-time reconfiguration, and heterogeneous distributed systems.



**Dirk Stroobandt** (S'92–M'98) received the Ph.D. degree in electrotechnical engineering from Ghent University, Ghent, Belgium, in 1998. He was a Visiting Researcher at the University of California at Irvine, Irvine, CA, USA, in 1997, and at the University of California at Los Angeles, Los Angeles, CA, USA, from 1999 to 2000. He is currently a Full Professor at the Computer Systems Laboratory, Department of Electronics and Information Systems, Ghent University, where he also leads the research group Hardware and Embedded Systems with inter-

ests in semiautomatic hardware design, run-time field-programmable gate array reconfiguration, and reconfigurable multiprocessor networks.



**Sebastián López** was born in Las Palmas de Gran Canaria, Spain, in 1978. He received the Electronic Engineering degree from the University of La Laguna, San Cristobal de La Laguna, Spain, in 2001, and the Ph.D. degree in electronic engineering from the University of Las Palmas de Gran Canaria, Las Palmas de Gran Canaria, in 2006. He is currently an Associate Professor with the University of Las Palmas de Gran Canaria, where he is involved in research activities with the Integrated Systems Design Division, Institute for Applied Microelectronics.

He has coauthored more than 120 articles in international journals and conferences. His research interests include real-time hyperspectral imaging, reconfigurable architectures, high-performance computing systems, and image and video processing and compression. Dr. López was a recipient of regional and national awards during his electronic engineering degree. He also serves as an Active Reviewer for different JCR journals and as a Program Committee Member of a variety of reputed international conferences. Furthermore, he acted as one of the program chairs of the IEEE Workshop on Hyperspectral Image and Signal Processing: Evolution in Remote Sensing (WHISPERS) in its 2014 edition and of the SPIE Conference of High Performance Computing in Remote Sensing, from 2015 to 2018. He is also an Associate Editor of the IEEE Journal of Selected Topics in Applied Earth Observations and Remote Sensing, MDPI Remote Sensing, and Mathematical Problems in Engineering Journal. He was an Associate Editor of the IEEE Transactions on Consumer Electronics, from 2008 to 2013. Moreover, he has been the Guest Editor of different special issues in JCR journals related with his research interests.



**María Díaz** was born in Spain, in 1990. She received the Industrial Engineering degree from the University of Las Palmas de Gran Canaria (ULPGC), Spain, in 2014, and the master's degree in system and control engineering imparted jointly by the *Universidad Complutense de Madrid* (UCM) and the *Universidad Nacional de Educación a Distancia* (UNED). She also received the Ph.D. degree from the ULPGC in 2021 where developed her research activities at the Integrated Systems Design Division of the Institute for Applied Microelectronics

(IUMA). Additionally, she conducted a research stay in the GIPSA-lab, University of Grenoble Alpes, France, and in the University of Castilla-La Mancha (UCLM), Spain. Her research interests include image and video processing, development of highly parallelized algorithms for hyperspectral images processing, and hardware implementation.



**Jesús Barba** received the MS and PhD degrees in Computer Engineering Diploma from the University of Castilla-La Mancha (UCLM), Spain, in 2001 and 2008 respectively. He is working as Associate Professor with the Department of Information and Systems Technology (TSI) since 2001 and member of the ARCO research group, located at the School of Computer Science (UCLM, Spain). Among the open research lines and interests it is worth mentioning the following: Low-cost & low power reconfigurable systems for ubiquitous computing, Reconfigurable

computing platforms for AI algorithms, Heterogeneous Distributed Embedded Computing and High-level Synthesis Tools.



**Juan Carlos López** received the M.S. and Ph.D. degrees in telecommunication (electrical) engineering from the Technical University of Madrid, in 1985 and 1989, respectively. From 1989 to 1999, he was an Associate Professor with the Department of Electrical Engineering, Technical University of Madrid. From September 1990 to August 1992, he was a Visiting Scientist with the Department of Electrical and Computer Engineering, Carnegie Mellon University, Pittsburgh, PA, USA. From 2000 to 2008, he has worked as the Dean of the School

of Computer Science, University of Castilla-La Mancha. He is currently a Professor of computer architecture with the University of Castilla-La Mancha. His research interests include embedded system design, distributed computing, and advanced communication services. Prof. Lopez is member of the IEEE and ACM. He is and has been a member of different panels of the Spanish National Science Foundation and the Spanish Ministry of Education and Science, regarding the Information Technologies research programs.